Robust Optimization for Multi-Energy Microgrid Sizing and Energy Management under Load Uncertainty with Demand Response

Mojtaba Hadi, Elhoussin Elbouchikhi, Zhibin Zhou, Abdelhakim Saim

Results in Engineering 29 (2026) 108609

Contents lists available at ScienceDirect

Results in Engineering

journal homepage: www.sciencedirect.com/journal/results-in-engineering

Research paper

Robust optimization for multi-Energy microgrid sizing and energy management under load uncertainty with demand response

Mojtaba Hadi [a,b,*], Elhoussin Elbouchikhi [c,*], Zhibin Zhou [d], Abdelhakim Saim [a]

[a] IREENA UR 4642, Nantes University, Saint-Nazaire, France
[b] LABISEN, ISEN OUEST, Nantes, France
[c] SATIE UMR CNRS 8029, CY Cergy-Paris University, Cergy-Pontoise, France
[d] LABISEN, ISEN OUEST, Brest, France

ARTICLE INFO

Keywords:
Multi-Energy microgrids
Sizing
Energy management system
Robsut optimization
CHP
Demand response.

ABSTRACT

The growing interdependence among electricity, heat, and gas networks creates significant challenges for achieving reliable and cost-efficient design and operation in Multi-Energy Microgrids (MEMGs). Conventional optimization approaches often treat these subsystems separately, focus on either design or operational scheduling in isolation, and ignore load uncertainty. As a result, it leads to inefficient resource utilization and higher overall costs. To address these issues, this study proposes a two-stage robust optimization framework for the design and energy management of a MEMG under power-load uncertainties. In the first stage, the framework uses a bi-objective model to determine the optimal sizes of key components—including the PV panel area, wind turbine radius, battery capacity, and gas allocation for the CHP unit—while accounting for uncertainty in power loads. The two objectives are: (i) maximizing the use of renewable and CHP resources, and (ii) minimizing the total system cost, which includes electricity, gas, emissions, operational, and demand-response costs. In the second stage, the optimized components are subsequently applied to an IEEE 14-bus MEMG test system, where a robust energy-management strategy coordinates power, heat, and gas flows under uncertain conditions using the Mixed-Integer Nonlinear Programming (MINLP) model. The results show that the robust strategy ensures all energy demands are met even under worst-case load variations. However, achieving this higher level of resilience increases electricity expenses by 21 %, emissions-related costs by 15 %, line losses by 0.8 %, and overall system cost by 6 %, while electricity exported to the main grid decreases by 17 %.

1. Introduction

A microgrid is a localized energy system capable of operating autonomously or in conjunction with the main grid, integrating distributed energy resources (DERs) such as solar panels, wind turbines, and energy storage systems. These systems offer numerous benefits, including reduced carbon emissions, enhanced energy security, and the capability to efficiently manage local energy demand [1]. As the global energy landscape shifts towards cleaner and more decentralized power generation, the deployment of microgrids is gaining significant traction.

Designing a microgrid is a complex and multifaceted task, primarily involving two key challenges: siting and sizing. Siting involves identifying the most suitable location for the microgrid, while sizing focuses on determining the optimal dimensions of its components, such as power capacity, energy storage, and the number of units [2]. Oversizing a microgrid can result in high costs and surplus energy production, whereas undersizing may lead to insufficient energy supply, causing power shortages [3]. To overcome these challenges and fully leverage the potential of renewable energy-based microgrids, it is essential to implement optimal sizing in conjunction with an effective energy management strategy [4]. The majority of existing approaches in the literature address the microgrid sizing problem as an optimization challenge, where the objective functions are primarily designed to reduce energy generation costs and environmental impact, while improving operational reliability [5,6]. As reviewed in [7], numerous methodologies have been proposed to address the sizing problem of hybrid microgrids in a variety of applications and scenarios.

Due to the inherently high volatility of renewable energy sources such as wind and solar power, their increasing integration introduces significant uncertainty into multi-microgrid (MMG) systems. In recent years, considerable research has focused on the optimal operation of MMG systems under uncertainty [8]. Among the most widely adopted

* Corresponding authors.
E-mail addresses: Hadi.mojtaba@etu.univ-nantes.fr (M. Hadi), elhoussin.elbouchikhi@cyu.fr (E. Elbouchikhi), zhibin.zhou@isen-ouest.yncrea.fr (Z. Zhou), abdelhakim.saim@univ-nantes.fr (A. Saim).

https://doi.org/10.1016/j.rineng.2025.108609
Received 18 September 2025; Received in revised form 26 November 2025; Accepted 4 December 2025
Available online 7 December 2025

Nomenclature

Abbreviations

BDC	Battery Degradation Cost
$BESS$	Battery Energy Storage Systems
CHP	Combined Heat and Power
Cl	Controllable loads
CV	Calorific Value for natural gas
$DERs$	Distributed Energy Resources
DHN	District Heating Network
DOD	Depth Of Discharge
$DRPs$	Demand Response Programs
ESS	Energy Storage Systems
GDS	Gas Distribution System
LCC	Life Cycle Cost
$LCOC$	Levelized Cost Of Cogeneration
$LCOE$	Levelized Cost Of Electricity
$MEMG$	Multi-Energy Microgrid
$MINLP$	Mixed-Integer Nonlinear Programming
PDS	Power Distribution System
POF	Pareto Optimal Front
PSO	Particle Swarm Optimization
$SCOPF$	Security Constrained Optimal Power Flow
SOC	State Of Charge
STC	Standard Test Conditions
SV	Residual Value
Uc	Uncontrollable loads

Parameters

α_l	Uncertainty radius for load uncertainty
β	Temperature coefficient
β_e, β_g	Emission factor for electricity and gas generation
β_l	Safeguard parameter for load uncertainty impact
χ_d^{Υ}	Impact of Depth of Discharge on cycle life
χ_T^{Υ}	Impact of temperature on cycle life
χ_T^{Ξ}	Temperature-dependent power fading coefficient
η_{w}, η_{PV}	Efficiency factors for the wind turbine and PV
η_b^+, η_b^-	Battery charging and discharging efficiency
$\eta_{e,app}$, $\eta_{g,app}$	Efficiency of electrical and heat appliances
η_{ge}, η_{gh}	Gas-to-electricity and heat conversion efficiency
η_{th^+}, η_{th^-}	Heat storage charging and discharging efficiency
Γ_l	Uncertainty budget defining the deviation range
$\lambda_e(t)$	Electricity price at time t
λ_g	Gas price
λ_{Dr}	Cost coefficient for demand response
λ_{Sell}	Price for selling electricity back to the grid
ρ	Air density
σ^s, σ^{w}	Degradation factor for PV and wind
Υ_{ref}	Rated cycle life of the battery
$C_{\mathrm{fuel},i}^{\mathrm{chp}}$	Fuel cost for CHP in year i
$C_{\mathrm{inv}}^{\mathrm{chp}}$	Investment cost for CHP system
$C_{\mathrm{om},i}^{\mathrm{chp}}$	Operation and maintenance costs for CHP in year i
C_{inv}^s, $C_{\mathrm{inv}}^{\mathrm{w}}$	Investment costs for PV and wind systems
C_{om}^s, $C_{\mathrm{om}}^{\mathrm{w}}$	Operation and maintenance costs for PV and wind
C_{inv}^b, C_{inv}^{th}	Investment costs of the battery and heat storage
C_{om}^b, C_{om}^{th}	Operational costs of the battery and heat storage
C_{CHP}	Levelized cost of cogeneration
C_{PV}, C_W	Levelized cost of electricity for PV and wind
dr_b, dr_{th}	Discount rates for the battery and heat storage
dr_S, dr_{w}	Discount rates for the PV and wond systems
E_b^0, H_{th}^0	Initial state of charge of the battery and heat storage
E_{CHP}^i	Electricity output of CHP in year i
E_{an}^s	Annual energy output for PV
E_{max}, Ξ_{ref}	Reference capacity of battery and thermal storage
G_d^t	Household gas demand at time t
H_{CHP}^{i}	Heat output of CHP in year i
H_d^t	Household heat demand at time t
l_{b+}^t, l_{b-}^t	Maximum battery charging and discharging rates
l_{th+}^t, l_{th-}^t	Maximum heat storage charging and discharging rates
P_{Uc}^t	Uncontrollable power loads at time t
R_i^{chp}	Revenue from by-products or subsidies in year i
T_{NOC}	Nominal operating cell temperature
T_{ref}	Reference temperature of the photovoltaic cell
$V_{Chp}^{\max}$	Maximum natural gas input for the CHP
$V_{Chp}^{\min}$	Minimum natural gas input for the CHP
$V_{\max}^i$, $V_{\min}^i$	Maximum and minimum voltage limit at bus i
y_{ij}	Admittance between buses i and j

Variables

C_B	Battery degradation cost
C_c	Emission costs
C_g	Cost of natural gas purchased from the grid
C_{Sell}	Selling surplus electricity to the main grid
G^t	Gas purchased from the grid at time t
H_{CHP}^t	Heat produced by the CHP system at time t
OC_b^t	Operational cost of the battery at time t
$P_{Uc}^{t,Ro}$	Worst-case uncontrollable load
$P_c(k,t)$	Load curtailed or shifted via DR
$P_{loss}^{ij,t}$	Line losses from bus i to bus j at time t
P_{Boiler}^t	Boiler heat generation at time t
P_{Grid}^t	Electricity purchased from the grid at time t
P_{PV}^t	PV power generated at time t
P_{Uc}^t	Uncontrollable power loads at time t
P_{b+}^t, P_{b-}^t	Battery charging and discharging power
R_{WT}	Radius of the wind turbine
SOC_b^t	State of charge of the battery at time t
T_a^t	Ambient temperature at time t
V_t^i	Voltage at bus i at time t
u_{es}^t, u_{th}^t	Binary variables for battery and heat storage
C_{Dr}	Implementation cost of demand response
C_e	Cost of electricity purchased from the grid
C_o	Operating costs
E_{CHP}^t	Electricity produced by the CHP at time t
G_{Boiler}^t	Gas consumed by the auxiliary boiler
$L_{DV}^{t,max}$	Maximum allowable demand variation
OC_{th}	Operational cost of the heat storage
P^k	Total energy consumption of customer k
P_t^i	Power injected at bus i at time t
P_{loss}^t	Total power loss at time t
P_{Cl}^t	Controllable power loads at time t
P_{Irr}^t	Solar irradiation at time t
P_{Sell}^t	Amount of electricity sold at time t
P_{WT}^t	Wind power generated at time t
$P_{th^+}^t$, $P_{th^-}^t$	Heat charged and discharged into storage
S_{PV}	Surface area of the PV panels
SOC_{th}^t	State of charge of the heat storage
V_{Chp}^t	Gas allocation to CHP at time t
$V_{\mathrm{w}}(t)$	Wind speed at time t
ξ_{load}^t	Auxiliary variable capturing potential load deviation at time t

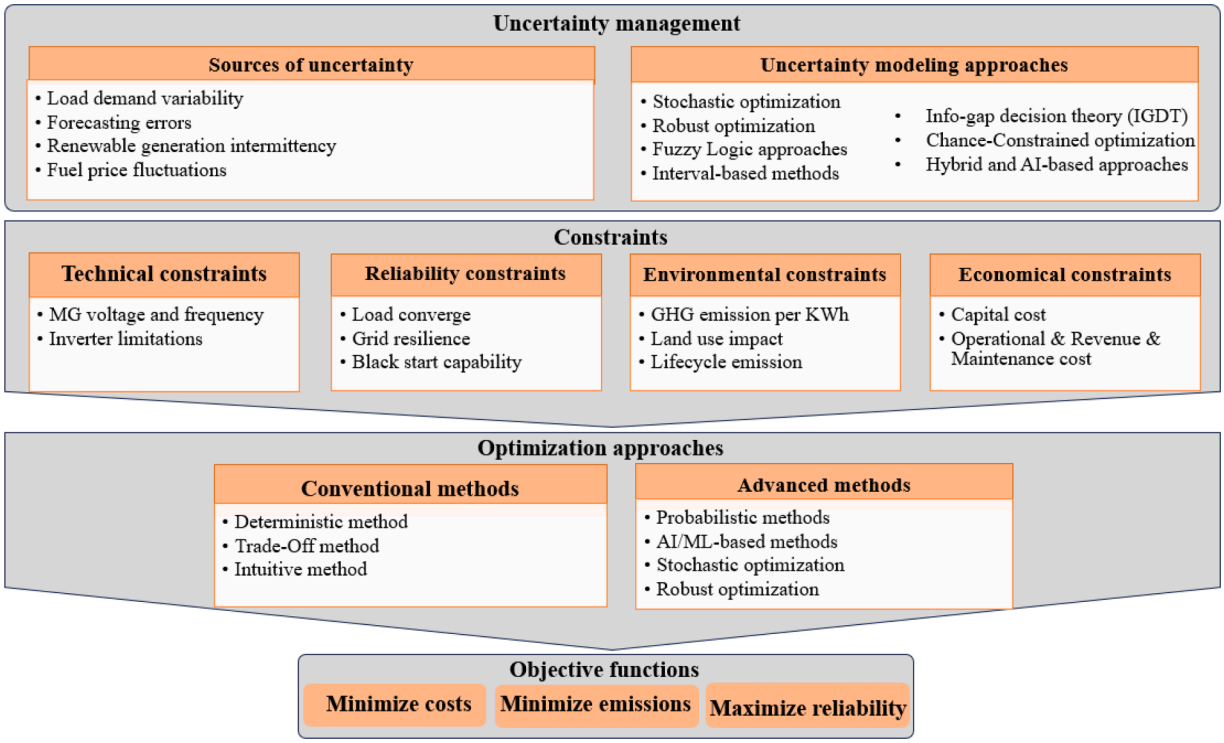

Fig. 1. Uncertainty management and sizing optimization in Microgrids.

approaches for handling uncertainty are Stochastic Programming (SP) and Robust Optimization (RO). SP relies on the assumption that the probability distribution of uncertain parameters, such as renewable generation and load, is known. However, in practice, obtaining accurate probability distributions is challenging, particularly in microgrids where data is limited and the geographic footprint is relatively small. In contrast, RO does not require any prior knowledge of probability distributions or correlations among uncertain parameters, making it a more practical and reliable approach for real-world microgrid applications [9]. By considering the role of uncertainty in sizing and energy management, Fig. 1 presents an overview of the uncertainty management frameworks and the methodologies used to address the sizing optimization problem.

In [10], the optimal energy management of MMG system was addressed using a stochastic multi-objective framework, where the uncertainty of renewable energy generation was captured through representative scenarios. A risk-averse energy management approach for networked microgrids was also formulated based on stochastic linear programming. In [11], a two-stage adaptive robust optimization model was proposed to handle the energy dispatch problem in multi-microgrid systems, enabling each microgrid to effectively manage local uncertainties. Furthermore, [12] introduced a two-stage robust optimization framework for the coordinated operation of electricity-gas-heat integrated multi-energy microgrids under both renewable and load uncertainties. By incorporating Power-to-Hydrogen-and-Heat (P2HH) systems along with the dynamic characteristics of gas and heat networks, the proposed model significantly improves operational flexibility and overall system efficiency. In [13], an optimization method is presented for Battery Energy Storage Systems (BESS) sizing in microgrids, solving the Security Constrained Optimal Power Flow (SCOPF) problem while accounting for stochastic forecasting errors in PV output. In [14], the authors proposed an integrated planning model to evaluate the techno-economic performance of a standalone microgrid powered by renewable energy sources. This model combines capacity sizing and operational scheduling while incorporating demand-side management strategies across diverse design scenarios, including wind turbines, photovoltaic systems, diesel generators, and energy storage solutions such as batteries and pumped thermal energy storage. The study in [15] focused on optimizing the sizing and allocation of Photovoltaic Distributed Generators (PVDG) and Energy Storage Systems (ESS) in islanded microgrids. The main objective is to increase energy reliability during disruptions while meeting energy demands and minimizing operational costs. In [16], a multi-objective optimization algorithm is introduced for the optimal sizing of standalone systems that incorporate PV panels, wind turbines, and battery energy storage systems. This algorithm accounts for critical factors such as power supply reliability, energy stability, energy utilization, and economic efficiency, ensuring a balanced and efficient design. In our previous work in [17], we investigated the optimal design of a multi-energy DC microgrid integrating multiple resources. The first objective was to determine the optimal PV panel surface area, wind turbine radius, and CHP gas allocation to maximize renewable energy utilization while minimizing total costs–including electricity, natural gas, emissions, and operations. The second objective was to analyze heat and power management strategies in selected scenarios.

Although recent studies have investigated the sizing of MG system components, to the best of the authors' knowledge, most have primarily focused on the integration and operation of solar PV, wind turbines, battery storage systems, and, in some cases, diesel generators–while largely overlooking the optimal sizing of CHP units within multi-energy microgrids. Additionally, although numerous studies address uncertainty at the operational level using robust optimization techniques, comprehensive investigations that incorporate uncertainty across both the design and operational stages of MEMG systems remain largely lacking. These gaps highlight the need for more integrated studies that examine component interdependencies and assess the impact of uncertainty on microgrid planning and resource scheduling. Table 1 offers a comprehensive comparison between previous research and the current study, emphasizing key distinctions and contributions. Building on this foundation, this work proposes an integrated framework that coordinates the power distribution system (PDS), district heating network (DHN), and gas distribution system (GDS) to meet multi-energy demands. The main contributions are summarized as follows:

Table 1
Review of previous studies for comparative analysis with the current research.

Ref	MEMG	Energy component sizing				Optimal indicators	Optimal scenario identification	DR	Robust optimisation in:	
		PV	Wind	ESS	CHP				Sizing	Operation
[9]	×	✓	×	✓	×	Economic, Environmental	✓	×	✓	✓
[13]	×	✓	×	✓	×	Reliability, Cost, Security	✓	×	✓	✓
[14]	✓	✓	✓	✓	×	Reliability, Environmental, Economic	✓	✓	×	×
[15]	×	✓	×	✓	×	Reliability, Environmental, Economic	×	×	✓	×
[17]	✓	✓	✓	×	✓	Reliability, Environmental, Economic	×	×	×	×
[18]	×	✓	✓	✓	×	Reliability, Environmental, Economic	✓	✓	×	×
[19]	×	✓	✓	×	×	Efficiency, Reliability	×	×	✓	×
[20]	×	✓	×	✓	×	LCOE, LCE, Peak shaving	✓	×	✓	✓
[21]	×	✓	✓	✓	×	Reliability, Economic	✓	×	×	×
[22]	×	×	✓	✓	×	Economic, Wind curtailment	✓	×	×	×
[23]	×	×	×	✓	×	Economic	×	×	✓	×
[24]	✓	✓	✓	✓	×	Economic, Resilience, Environmental	✓	✓	✓	×
[25]	×	✓	✓	✓	×	Economic, Environmental, Reliability	✓	×	✓	×
[26]	×	✓	✓	✓	×	Economic, Reliability	✓	×	✓	×
[27]	×	✓	×	✓	×	Economic, Environmental	✓	×	×	×
[28]	×	✓	✓	✓	×	Reliability, Economic	×	×	×	×
[29]	✓	×	×	×	✓	Reliability, Economic	×	✓	×	×
[30]	×	✓	×	✓	×	Economic, Peak shaving	✓	×	✓	✓
[31]	×	✓	✓	✓	×	Economic, Environmental	✓	×	×	×
[32]	×	✓	✓	✓	×	Economic, Reliability	✓	✓	✓	✓
This study	✓	✓	✓	✓	✓	Reliability, Environmental, Economic	✓	✓	✓	✓

- Comprehensive robust microgrid sizing framework: A bi-objective robust optimization framework is developed to determine the optimal sizing of PV surface area, wind turbine radius, battery storage capacity, and gas allocation to the CHP unit, while explicitly considering uncertainties associated with uncontrollable power loads.
- Robust energy management implementation: The optimal sizing of the design variables achieved in the previous stage are applied to the IEEE 14-bus system. A robust optimization strategy is subsequently implemented to ensure reliable energy supply and demand fulfillment under worst-case power load uncertainty scenarios.
- Demand response integration: Price-based and incentive-based demand response programs are incorporated to evaluate their impacts on cost reduction, load shifting, and overall system efficiency within the IEEE 14-bus framework.

The remainder of this manuscript is structured as follows: Section II presents the system architecture and modeling framework. Section III discusses the simulation setup and corresponding results. Finally, Section IV concludes the paper and outlines potential directions for future research.

2. System architecture and modeling

This paper presents a system architecture that integrates a PDS, a DHN, and a GDS, powered by a diverse mix of energy sources and storage systems. The PDS integrates PV panels, wind turbine, batteries, CHP unit, and the main electrical grid. On the consumption side, electrical loads are categorized as controllable and uncontrollable. In the DHN, heat loads are supplied by CHP unit, discharges from thermal storage, and direct natural gas supply from the main gas grid, such as through a boiler. Excess heat is stored in a thermal storage system and utilized during peak demand periods. The GDS is fueled by natural gas from the main gas grid, which is used to power CHP unit, operate heat generator (e.g., boiler), and address the requirements of gas-based applications excluding heating. Fig. 2 provides a detailed illustration of the microgrid architecture used for sizing.

2.1. Constraints

The model incorporates detailed constraints for the PV system, wind turbines, lithium-ion battery storage, and thermal energy storage. It also includes constraints for the CHP unit, along with system reliability requirements. Additionally, the model accounts for demand response strategies and applies robust optimization to improve performance under uncertainty.

2.1.1. PV System

The power generated by a PV installation can be calculated based on temperature and solar irradiation using the following equation [33]:

$$P_{PV}^{t} = S_{PV} \cdot \eta_{PV} \cdot P_{Irr}^{t} \cdot \left(1 - \beta \cdot \left(T_{a}^{t} - T_{ref} + \frac{T_{NOC} - 20}{800} \cdot P_{Irr}^{t}\right)\right), \quad 1 \le t \le 24\,\mathrm{h} \tag{1}$$

Where, P_{PV}^{t} denotes the power output of the PV system at time t, which is influenced by several factors. S_{PV} is the total surface area of the PV array, and η_{PV} represents the overall system efficiency, accounting for both technological performance and power conditioning losses. P_{Irr}^{t} refers to the solar irradiance at time t. The parameter β is the temperature coefficient, indicating how sensitive the PV output is to temperature variations. T_{a}^{t} is the ambient temperature at time t, T_{ref} is the reference temperature of the PV cells, and T_{NOC} denotes the nominal operating cell temperature under standard conditions. The PV system's operational cost, OC_{s}^{t}, is provided by:

$$OC_{s}^{t} = C_{PV} \cdot P_{PV}^{t}, \quad t \in T \tag{2}$$

The Levelized Cost of Electricity (LCOE) is a standard metric used to evaluate the cost of electricity generation over a system's lifespan. For PV system, the LCOE, denoted as C_{PV}, is calculated using Eq. (3) [33]:

$$C_{pv} = \frac{C_{inv}^{s} + \sum_{i=1}^{n} C_{om}^{s}(1 + dr_{s})^{-i}}{\sum_{i=1}^{n} E_{an}^{s}(1 - \sigma^{s})^{i-1}(1 + dr_{s})^{-i}} \tag{3}$$

This formulation incorporates the investment cost (C_{inv}^{s}), which includes expenses related to PV modules, converters, installation, land acquisition, and balance-of-system components, along with the annual maintenance cost (C_{om}^{s}) and the annual energy output (E_{an}^{s}). The annual energy output is computed by summing the hourly average solar power across the year, then discounting it over n years at the rate dr_{s}. To reflect system performance degradation over time, a degradation factor σ^{s} is applied to E_{an}^{s} starting from the second year.

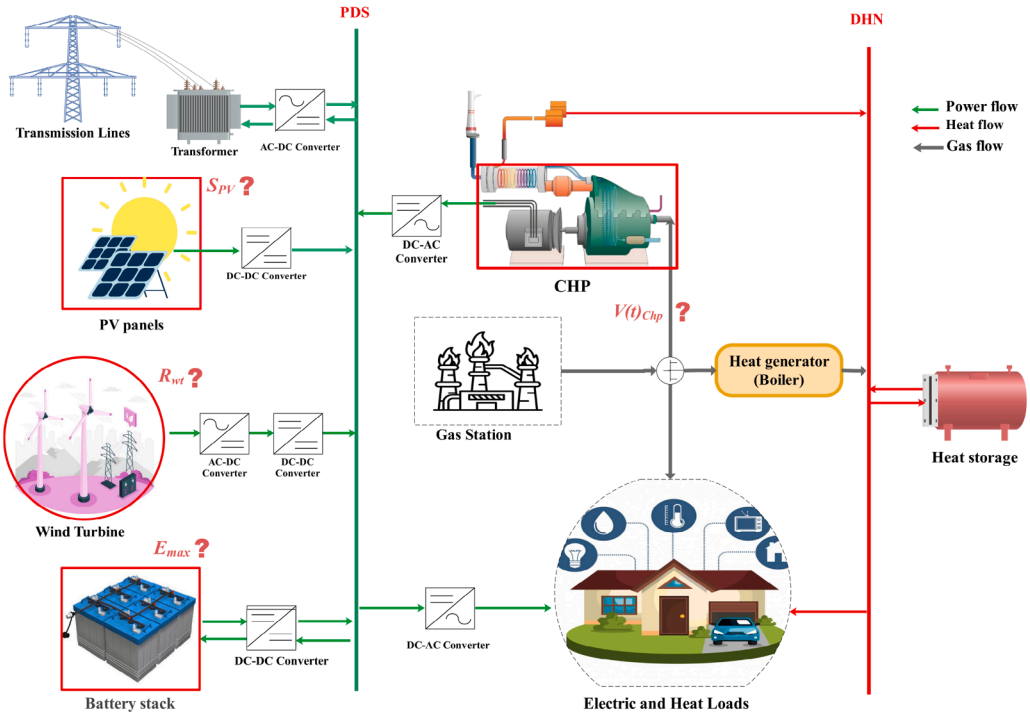

Fig. 2. System structure considered for sizing.

2.1.2. Wind system

The electrical power output of a wind turbine can be expressed as [34]:

$$P_{WT}^{t} = \begin{cases} 0, & V_w < v_{cut\text{-}in} \\ \frac{1}{2}\eta_w \rho \pi R_{WT}^2 V_w(t)^3, & v_{cut\text{-}in} \le V_w \le v_r \\ \frac{1}{2}\eta_w \rho \pi R_{WT}^2 v_r^3, & v_r \le V_w \le v_{cut\text{-}out} \\ 0, & V_w > v_{cut\text{-}out} \end{cases} \tag{4}$$

Where, P_{WT}^{t} is the wind power output at time t, while η_w is the power coefficient representing conversion efficiency. ρ denotes the air density, and R_{WT} is the radius of the wind turbine blades. $V_w(t)$ denotes the wind speed at time t, which directly influences the wind turbine's power output. The turbine begins operating at the cut-in wind speed, $v_{cut\text{-}in}$, and the output power increases with wind speed up to the rated speed, v_r. Beyond this point, as wind speed continues to rise, the power output remains constant at its rated value. If the wind speed exceeds the cut-out threshold, $v_{cut\text{-}out}$, the turbine automatically shuts down to prevent damage and ensure operational safety. The operational cost of the wind turbine and the LCOE for wind power are modeled as follows:

$$OC_W^t = C_W \cdot P_{WT}^t, \quad t \in T, \tag{5}$$

$$C_W = \frac{C_{inv}^w + \sum_{i=1}^{n} C_{om}^w (1+dr_w)^{-i}}{\sum_{i=1}^{n} E_{an}^w (1-\sigma^w)^{i-1}(1+dr_w)^{-i}} \tag{6}$$

Where, OC_W^t represents the operational cost at time t, and C_W denotes the LCOE for wind power. This metric accounts for several components, including the investment cost (C_{inv}^w), maintenance cost (C_{om}^w), annual energy output (E_{an}^w), discount rate (dr_w), and the degradation factor of the wind turbine (σ^w).

2.1.3. Lithium-ion battery

Due to the unpredictable nature of renewable energy sources and the frequent mismatch between demand and supply, incorporating batteries and heat storage systems becomes essential. These systems are subject to constraints on charging capacity, recharge and discharge rates, and State Of Charge (SOC) at each time step t [35].

$$P_{b+}^t \le l_{b+}^t \cdot E_{max} \cdot u_{es}^t, \quad t \in T \tag{7}$$

$$P_{b-}^t \le l_{b-}^t \cdot E_{max} \cdot (1-u_{es}^t), \quad t \in T \tag{8}$$

$$SOC_b^t = \frac{E_b^0}{E_{max}} + \sum_{h=1}^{t} \left(\eta_{b+} P_{b+}^h - \frac{P_{b-}^h}{\eta_{b-}} \right) \cdot \frac{\Delta h}{E_{max}} \tag{9}$$

Where, l_{b+}^t and l_{b-}^t represent the maximum charging and discharging rates of the battery per hour, respectively. The binary variable u_{es}^t ensures that charging and discharging do not occur simultaneously. The term E_{max} denotes the reference battery storage capacity. The state of charge SOC_b^t is determined based on the initial battery energy level at the start of the day (E_b^0) and the cumulative effect of charging (P_{b+}^t) and discharging (P_{b-}^t) processes up to time t. The Battery Degradation Cost (BDC) model for lithium-ion batteries accounts for the impacts of temperature and Depth of Discharge (DOD) on both the energy capacity and the cycle life of the battery. In Eqs. (10) and (11), OC_b^t and C_B represent the operational cost and BDC, respectively [36]:

$$OC_b^t = C_B \left(\eta_{b+} P_{b+}^t + \frac{P_{b-}^t}{\eta_{b-}} \right), \quad t \in T \tag{10}$$

$$C_B = \frac{1}{2} \frac{\left[C_{inv}^b + \sum_{t=1}^{n} C_{om}^b (1+dr_b)^{-t} \right] (1+dr_b)^n - SV}{(1+dr_b)^n \chi_T^{\Xi} \chi_T^{\Upsilon} \chi_d^{\Upsilon} \Upsilon_{ref} E_{max}}. \tag{11}$$

Where, η_{b+} and η_{b-} represent the battery's charging and discharging efficiencies, while C_{inv}^b denotes its investment cost. The parameter χ_T^{Ξ} is the normalized temperature-dependent power-fading coefficient, and χ_T^{Υ} and χ_d^{Υ} capture the effects of temperature and DOD on battery cycle life, respectively. The residual value (SV) reflects the remaining economic value of the battery at the end of its service life [37]. Finally, C_{om}^b represents the annual operation and maintenance cost, and dr_b is the discount rate used to compute present-value costs.

2.1.4. Heat storage system

A heat storage system is a technology used to store thermal energy for later use, enabling more efficient energy management in heating and cooling applications. These systems can utilize various storage media such as water, molten salts, or phase change materials. They are widely integrated into renewable energy systems, such as solar thermal or CHP

units, to enhance overall efficiency, reduce energy costs, and improve grid stability by balancing supply and demand fluctuations [38]. Similar to battery storage, thermal energy storage is subject to operational constraints. The charging and discharging limits, as well as the SOC, are defined as follows:

$$P^t_{th+} \le I^t_{th+} \cdot u^t_{th} \cdot \Xi_{ref} \tag{12}$$

$$P^t_{th-} \le I^t_{th-} \cdot (1 - u^t_{th}) \cdot \Xi_{ref} \tag{13}$$

$$SOC^t_{th} = \frac{H^0_{th}}{\Xi_{ref}} + \sum_{h=1}^{t} \left(P^h_{th+} \cdot \eta_{th+} - \frac{P^{h-}_{th-}}{\eta_{th-}} \right) \cdot \frac{\Delta h}{\Xi_{ref}} \tag{14}$$

In these equations, P^t_{th+} and P^t_{th-} denote the thermal charging and discharging power at time t, respectively. The parameters I^t_{th+} and I^t_{th-} represent the maximum allowable charging and discharging rates per time step. The binary variable u^t_{th} determines the operating mode of the thermal storage system, ensuring that charging and discharging cannot occur simultaneously. Specifically, $u^t_{th} = 1$ allows charging, while $u^t_{th} = 0$ allows discharging. The term Ξ_{ref} is the reference thermal storage capacity used for scaling purposes. The variable SOC^t_{th} indicates the state of charge at time t, with H^0_{th} representing the initial SOC. The parameters η_{th+} and η_{th-} are the thermal charging and discharging efficiencies, respectively. Degradation in thermal energy storage systems is often minimal, particularly in sensible heat storage technologies such as molten salt systems. These systems are known for their long cycle life and stable performance over time, so degradation is typically neglected in the optimization model [39]. As such, the cost modeling primarily includes the initial investment cost C^{th}_{inv}, the operation and maintenance cost C^{th}_{om}, and a discount rate dr_{th}. Over a total planning horizon of n time periods, the overall operational cost of the thermal storage is expressed as:

$$OC_{th} = C^{th}_{inv} + \sum_{t=1}^{n} \frac{C^{th}_{om}}{(1 + dr_{th})^t} \tag{15}$$

2.1.5. Network constraints

In a DC microgrid system, monitoring voltage levels at each bus and accounting for system losses are crucial for optimizing the scheduling of generation sources and implementing demand response strategies. The injection of power in each bus i is governed by the power flow equation in (16), which describes the relationship between voltage levels and line admittances throughout the network. The voltage at each bus is constrained within defined lower and upper bounds to ensure stable operation, as presented in Eq. (17). Additionally, line losses, which depend on the voltage differences between connected buses, are determined by Eq. (18). The overall impact of these line losses on the system is represented as total system losses at time t, as defined in Eq. (19). Collectively, these equations establish a comprehensive framework for managing power flow dynamics and loss optimization in DC microgrid [36].

$$P^t_i = \sum_{\substack{j=1 \\ j \ne i}}^{N} V^i_t \left(V^i_t - V^j_t \right) y_{ij}, \quad i \in \mathcal{N}, \tag{16}$$

$$V^i_{\min} \le V^i_t \le V^i_{\max}, \quad i \in \mathcal{N}, \tag{17}$$

$$P^{ij,t}_{loss} = \left(V^i_t - V^j_t \right)^2 y_{ij}, \quad j \ne i, \quad (i,j) \in \mathcal{N}, \quad t \in T, \tag{18}$$

$$P^{\mathrm{t}}_{loss} = \sum_{i=1}^{N-1} \sum_{j=i+1}^{N} P^{ij,t}_{loss}, \quad t \in T. \tag{19}$$

2.1.6. Boiler and CHP system

A boiler is a thermal device that converts the chemical energy of fuel–typically natural gas–into useful heat for space or water heating applications. The thermal output of the boiler at time t is calculated as:

$$P^t_{Boiler} = G^t_{Boiler} \cdot \eta_{g,app} \cdot CV \tag{20}$$

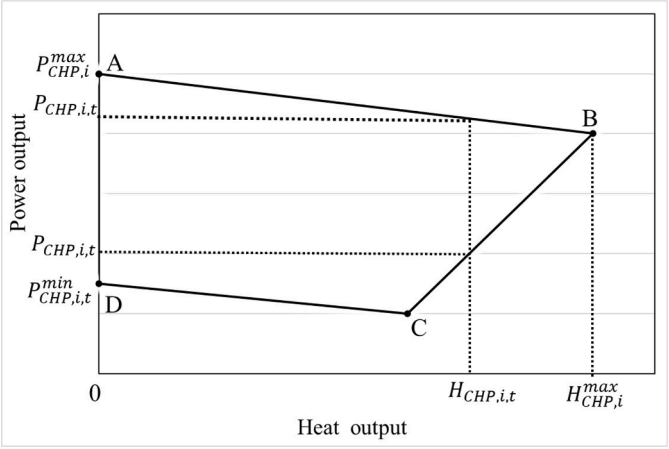

Fig. 3. Feasible operating region of a CHP unit.

Where, G^t_{Boiler} denotes the natural gas consumption at time t, $\eta_{g,app}$ is the apparent thermal efficiency of the boiler, and CV represents the calorific value of the natural gas. Unlike boilers, CHP systems simultaneously generate electricity and heat from a single energy source, significantly improving overall efficiency by capturing and utilizing waste heat that would otherwise be lost. The electricity produced by CHP units is supplied to the power grid, while the generated heat is used to meet thermal demand [40]. Fig. 3 illustrates the feasible operating region of a CHP unit, where the boundaries AD, AB, BC, and CD denote the minimum steam injection limit, maximum heat generation rate, upper fuel injection limit, and maximum power output limit, respectively [41]. Under high thermal demand conditions, the CHP unit operates mainly along boundary BC, producing excess electricity as a byproduct of heat generation. The feasible region for electricity (E_{CHP}) and heat (H_{CHP}) output can be mathematically represented by the following linear inequalities:

$$\begin{bmatrix} A_{CHP} & B_{CHP} \end{bmatrix} \begin{bmatrix} E_{CHP} \\ H_{CHP} \end{bmatrix} \le D_{CHP} \tag{21}$$

Where, A_{CHP} and B_{CHP} are coefficients defining the boundary slopes, and D_{CHP} is a vector of constants characterizing the limits of the feasible operating region. The electricity and heat generated by the CHP unit at time t are modeled as:

$$E^t_{CHP} = V^t_{Chp} \cdot CV \cdot \eta_{ge}, \tag{22}$$

$$H^t_{CHP} = V^t_{Chp} \cdot CV \cdot \eta_{gh}, \tag{23}$$

$$V^{min}_{Chp} \le V^t_{Chp} \le V^{max}_{Chp}, \tag{24}$$

In Eqs. (22) and (23), V^t_{Chp} denotes the volume of natural gas input to the CHP unit at time t, and η_{ge} and η_{gh} are the conversion efficiencies from gas to electricity and gas to heat, respectively. The fuel input is constrained within an allowable operating range as expressed in Eq. (24), where $V^{\min}_{Chp}$ and $V^{\max}_{Chp}$ indicate the minimum and maximum allowable gas input to the CHP system. The operational cost of the CHP unit at time t is given by:

$$OC^t_{CHP} = C_{CHP} \cdot \left(E^t_{CHP} + H^t_{CHP} \right) \tag{25}$$

where, C_{CHP} denotes the Levelized Cost Of Cogeneration (LCOC), which represents the cost per unit of total energy–comprising both electricity and heat–produced by the CHP system. The LCOC is defined as [42]:

$$C_{CHP} = \frac{C^{chp}_{inv} + \sum_{i=1}^{n} \left(C^{chp}_{om,i} + C^{chp}_{fuel,i} - R^{chp}_i \right) (1 + dr_{chp})^{-i}}{\sum_{i=1}^{n} \left(E^i_{CHP} + H^i_{CHP} \right) (1 + dr_{chp})^{-i}} \tag{26}$$

In this expression, C^{chp}_{inv} is the initial investment cost of the CHP unit, $C^{chp}_{om,i}$ and $C^{chp}_{fuel,i}$ are the operation and maintenance and fuel costs in year

i, respectively. R_i^{chp} refers to the revenue from by-products or incentives. E_{CHP}^i and H_{CHP}^i are the annual electricity and heat outputs, dr_{chp} is the discount rate, and n denotes the lifetime of the system in years.

2.1.7. Meeting power, heat, and gas demands

Stability in a MEMG refers to its ability to continuously and reliably supply electricity, heat, and gas under varying conditions. This stability is ensured by the power, heat, and gas balance constraints. The power balance equation is expressed as follows:

$$P_{Grid}^t + E_{CHP}^t + P_{PV}^t + P_{WT}^t + P_{b^-}^t \cdot \eta_{b^-} = \frac{P_{Cl}^t + P_{Uc}^t}{\eta_{e,app}} + \frac{P_{b^+}^t}{\eta_{b^+}} + P_{Sell}^t + P_{loss}^t \tag{27}$$

In this equation, P_{Grid}^t is the electrical power purchased from the main grid, P_{PV}^t and P_{WT}^t are the generated powers from photovoltaic panels and wind turbines, respectively. $P_{b^-}^t$ and $P_{b^+}^t$ denote the battery discharging and charging power, with η_{b^-} and η_{b^+} as their respective efficiencies. P_{Cl}^t and P_{Uc}^t represent the power consumption of controllable and uncontrollable appliances, scaled by the appliance efficiency $\eta_{e,app}$. P_{Sell}^t is the power sold to the grid, and P_{loss}^t accounts for distribution losses. The heat balance is given by:

$$H_{CHP}^t + P_{th^-}^t \cdot \eta_{th^-} + P_{Boiler}^t = H_d^t + \frac{P_{th^+}^t}{\eta_{th^+}} \tag{28}$$

Where, H_{CHP}^t is the thermal power produced by the CHP system, $P_{th^-}^t$ and $P_{th^+}^t$ are the discharging and charging powers of the heat storage system, and η_{th^-} and η_{th^+} are their respective efficiencies. P_{Boiler}^t is the heat provided by the auxiliary boiler, and H_d^t is the total thermal demand at time t. Finally, the gas balance is provided by:

$$G^t = G_d^t + V_{chp}^t + G_{Boiler}^t \tag{29}$$

In this constraint, G^t is the gas purchased from the main gas grid, G_d^t represents the portion of gas consumption used for non-thermal purposes, V_{Chp}^t is the volume of natural gas consumed by the CHP unit, and G_{Boiler}^t is the gas used by the auxiliary boiler.

2.1.8. Demand response programs

Demand Response Programs (DRPs) are typically categorized into two main types: incentive-based programs, which offer financial rewards to consumers who reduce or shift their electricity usage during peak demand periods, and price-based programs, which employ time-varying electricity tariffs to influence consumption behavior [43]. In this study, electrical loads are classified as either controllable or uncontrollable. Controllable loads can be scheduled or shifted to off-peak hours, helping to reduce energy costs and ease the burden on the power grid. A price-based DRP is implemented by introducing three distinct tariff levels over a 24-hours period. Consumers adjust their energy consumption in response to these tariffs. The implementation of demand response is subject to certain constraints. Eqs. (30) and (31) define the total controllable electricity consumption of customer k over the entire time horizon, along with its corresponding upper and lower bounds.

$$P^k = \sum_t P_c(k,t), \tag{30}$$

$$P_{\min}^k \le P^k \le P_{\max}^k, \tag{31}$$

where, $P_c(k,t)$ represents the controllable power demand of customer k at time t, which may be curtailed or shifted in response to the price signals. The bounds $P_{\min}^k$ and $P_{\max}^k$ define the acceptable daily consumption limits for customer k. The total controllable power demand across all customers at each time t is computed as:

$$P_{Cl}^t = \sum_k P_c(k,t), \tag{32}$$

$$P_{Cl}^{t,\min} \le P_{Cl}^t \le P_{Cl}^{t,\max}, \tag{33}$$

where, P_{Cl}^t is the aggregate controllable load at time t, and $P_{Cl}^{t,\min}$ and $P_{Cl}^{t,\max}$ represent the lower and upper bounds of allowable controllable demand at that time. This formulation ensures that demand shifts occur within realistic and predefined flexibility ranges while contributing to system-level optimization.

2.1.9. Robust optimization formulation for load uncertainty

The robust optimization framework used to manage power-load uncertainty is presented in Fig. 4. This framework combines various prediction techniques–including historical load data, weather conditions, electricity prices, and occupancy profiles–to construct an uncertainty set that reflects potential variations in system parameters. The feasible solution space is divided into two regions: a secure zone, where solutions remain feasible under all scenarios, and a risky zone, where violations may occur. The robust optimization approach ensures that operational decisions stay feasible and cost-efficient even under the worst-case deviations.

In this study, we focus specifically on the uncertainty associated with uncontrollable loads. We define α_l as the uncertainty radius, $L_{DV}^{t,max}$ as the maximum allowable demand variation at time t, and P_{Uc}^t as the deterministic load component unaffected by uncertainty. Based on these parameters, the possible range for the uncertain load $P_{Uc}^{t,new}$ is defined as:

$$P_{Uc}^t - \left(\alpha_l \cdot L_{DV}^{t,max} \cdot P_{Uc}^t\right) \le P_{Uc}^{t,new} \le P_{Uc}^t + \left(\alpha_l \cdot L_{DV}^{t,max} \cdot P_{Uc}^t\right) \tag{34}$$

Since robust optimization accounts for the worst-case scenario, the uncontrollable load under uncertainty, denoted by $P_{Uc}^{t,Ro}$, is defined as:

$$P_{Uc}^{t,Ro} = P_{Uc}^t + \alpha_l \cdot L_{DV}^{t,max} \cdot P_{Uc}^t \tag{35}$$

To quantify the cost associated with incorporating robustness into the model, we introduce the additional term C_{Robust}, which captures the expense of protecting against potential load deviations:

$$min\left\{ C_{Robust} = \sum_{t>1} \xi_{load}^t + \Gamma_l \cdot \beta_l \right\} \tag{36}$$

Subject to:

$$\xi_{load}^t + \beta_l \ge \alpha_l \cdot L_{DV}^{t,max} \cdot P_{Uc}^t, \quad \forall t > 1 \tag{37}$$

Where, the variable ξ_{load}^t serves as an auxiliary term capturing the potential deviation in load at time t. The parameter Γ_l defines the uncertainty budget, restricting the number of time periods subject to worst-case deviations. Additionally, the variable β_l serves as a safeguard by bounding the overall impact of load uncertainty.

2.2. Objective functions

Considering that the objectives of this research include both system sizing and energy management, two sets of objective functions are formulated.

2.2.1. Objective functions for optimal components

sizing Two objective functions are defined to determine the optimal sizing of the system components. The first objective, denoted as C_1, aims to minimize the total system cost, which comprises electricity and natural gas expenses, emissions cost, operational cost, and demand response program cost. Eq. (38) presents the formulation of C_1 and its components.

$$min\left\{C_1 = C_e + C_g + C_c + C_o + C_{Dr} - C_{Sell}\right\} \tag{38}$$

Where, C_e represents the cost of electricity imported from the main power grid, and C_g denotes the cost of natural gas purchased from the main gas network. The term C_c accounts for emissions-related costs arising from both electricity and gas consumption. C_o refers to operating costs, including the expenses associated with the operation of the PV system, wind turbine, CHP unit, battery, and thermal energy storage system. The cost related to participation in demand response programs is represented by C_{Dr}, while C_{Sell} captures the revenue generated from

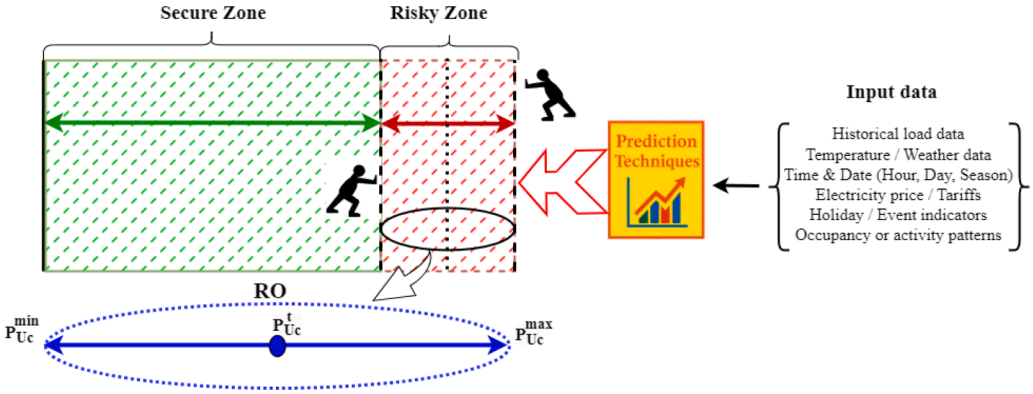

Fig. 4. Foundations and Conceptual Framework of Robust Optimization.

selling excess electricity back to the grid. Each of these cost components is defined as follows: [44,45]:

$$C_e = \sum_t (\lambda_e(t) \cdot P^t_{Grid}) \cdot \Delta t \tag{39}$$

$$C_g = \sum_t (\lambda_g \cdot G^t) \cdot \Delta t \tag{40}$$

$$C_c = \sum_t \left((1-\beta_e) \cdot P^t_{Grid} + (1-\beta_g) \cdot G^t \right) \cdot \Delta t \tag{41}$$

$$C_{Dr} = \sum_k \sum_t (\lambda_{Dr} \cdot P_c(k,t)) \cdot \Delta t \Delta k \tag{42}$$

$$C_{Sell} = \sum_t (\lambda_{Sell} \cdot P^t_{Sell}) \cdot \Delta t \tag{43}$$

$$C_o = \sum_t (OC^t_s + OC^t_W + OC^t_{CHP} + OC^t_b) \cdot \Delta t + OC_{th} \tag{44}$$

The second objective, denoted as C_2, aims to maximize the contribution of distributed energy resources, including PV, wind power, battery storage, and CHP system, as formulated in Eq. (45).

$$max \left\{ C_2 = \sum_t P^t_{PV} \cdot \Delta t + \sum_t P^t_{WT} \cdot \Delta t + \sum_t \left(E^t_{CHP} + H^t_{CHP} \right) \cdot \Delta t + \sum_t \left(P^t_{b+} + P^t_{b-} \right) \cdot \Delta t \right\} \tag{45}$$

To achieve these objectives, the optimal sizing of critical components–including the surface area of PV panels (S_{PV}), the radius of wind turbine (R_{WT}), the battery storage capacity (E_{max}), and the allocation of natural gas for the CHP system ($\sum V^t_{Chp}$)– is determined.

2.2.2. Objective functions for energy management

After determining the optimal system sizing, the energy management strategy is applied to the IEEE 14-bus configuration, where line losses are also taken into account. As a result, the objective function, presented in Eq. (46), is formulated to be minimized.

$$min\{C_1 = C_e + C_g + C_c + C_o + C_{Dr} + C_{Loss} - C_{Sell}\} \tag{46}$$

Where, C_{Loss} represents the total losses in the power distribution system, which is defined as follows:

$$C_{Loss} = \sum_t P^t_{loss} \cdot \Delta t \tag{47}$$

3. Numerical simulations

Based on the objective functions and constraints defined in the preceding section, and using the subsequent data, this section presents the simulation results and analyzes the performance of the proposed optimization framework.

3.1. Input data for sizing and energy management system

Table 2(a) summarizes the forecasted daily profiles of temperature, solar irradiation, and wind speed for a representative day. The technical specifications of the PV and wind systems, CHP unit, battery storage, heat storage, and both the gas and electricity networks are provided in Table 2(b). Additionally, Fig. 5 illustrates the daily variations in household energy demands. Fig. 5(a) presents the heat and gas load profiles, while Fig. 5(b) shows the uncontrollable and controllable loads, where the shaded area indicates the flexible range available for demand-side management.

3.2. Simulation results

The primary goals of the simulations are categorized into three main areas:

- Determining the robust optimal sizing of S_{PV}, R_{WT}, E_{max}, and $\sum V^t_{Chp}$ across various scenarios, while accounting for the uncertainty associated with uncontrollable power loads. This optimization is conducted based on the system architecture presented in Fig. 2 and governed by Eqs. (38) to (45).
- Implementing integrated management strategies for power, heat, and gas in the IEEE 14-bus system, which relies on the optimal values of S_{PV}, R_{WT}, E_{max}, and $\sum V^t_{Chp}$. Power load uncertainty is addressed through robust optimization to ensure all energy demands are reliably met, even under worst-case scenarios.
- Assessing the effectiveness of demand response programs in reducing costs and shifting loads.

3.2.1. Sizing and identifying the optimal scenario

The goal is to optimize the microgrid sizing by achieving two objectives: minimizing C_1 and maximizing C_2, simultaneously. Unlike single-objective optimization, which provides a single optimal solution, multi-objective optimization generates a set of optimized solutions. Each solution represents a specific scenario, collectively forming the pareto front, which illustrates the trade-offs between competing objectives. Fig. 6 illustrates the pareto front for the studied optimization problem.

Figs. 7(a) and (b) effectively illustrate the impact of variations in decision variables on the objective functions. The results show that increasing the values of S_{PV}, R_{WT}, E_{max}, and $\sum V^t_{Chp}$ leads to an increase in both C_1 and C_2. However, the growth rate of C_2 exceeds that of C_1, reflecting the stronger impact of these variables on the second objective. Furthermore, the results indicate that, given the problem's constraints, the CHP unit is utilized first, followed by the activation of the PV system starting from scenario 4. Battery storage (E_{max}) and wind power (R_{WT}) begin to contribute from scenario 10 onward.

As previously mentioned, C_1 comprises several cost components, including C_e, C_g, C_c, C_o, C_{Dr}, and C_{Sell}. Variations in S_{PV}, R_{WT}, E_{max},

Table 2
Practical data for simulation scenarios.

(a) Forecasted data [46].

Time (h)	Wind speed (m/s)	Temperature ($T_a(t)$) (°C)	Irradiation (P_{Irr}) (kW/m^2)
1	10.5	24.7	0.00000
2	13.5	24.5	0.00000
3	14.9	24.3	0.00000
4	15.6	24.4	0.00000
5	17.5	24.5	0.00000
6	18.6	26.5	0.00000
7	14.4	27.5	0.03000
8	14.1	28.0	0.06357
9	11.3	28.5	0.11000
10	9.7	28.8	0.28320
11	7.0	29.0	0.55040
12	5.9	29.7	0.78621
13	8.9	29.8	0.96207
14	9.5	30.0	1.02000
15	10.4	29.8	1.02000
16	8.8	29.5	1.00000
17	7.1	29.0	0.85256
18	8.3	27.7	0.63306
19	9.9	26.5	0.21191
20	7.5	24.8	0.00000
21	8.8	25.0	0.00000
22	9.8	24.8	0.00000
23	9.2	24.6	0.00000
24	8.4	24.8	0.00000

(b) Technical data [47–50].

Gas and Electricity Grids			
λ_e (€/kWh)	0.2, 0.25, 0.29	λ_g (€/kWh)	0.1
β_e	0.3	β_g	0.8
λ_{Dr}(€/kWh)	0.13	λ_{Sell}(€/kWh)	0.12
$V_i^{\max}$(V)	240	$V_i^{\min}$(V)	190
CHP System			
η_{ge}	0.30	η_{gh}	0.40
V_{Chp}^{max}	20 m^3	V_{Chp}^{min}	0 m^3
CV(kWh/m^3)	9.8	dr_{chp}	0.05
$C_{\text{inv}}^{\text{chp}}$ (€/kwh)	550	$C_{\text{om},i}^{\text{chp}}$ (€/year)	10
$C_{\text{fuel},i}^{\text{chp}}$ (€/year)	4	R_i^{chp} (€/year)	5
E_{CHP}^i (kWh/year)	2000	H_{CHP}^i (kWh/year)	3000
PV and wind systems			
η_{PV}	0.117	β	0.004
T_{ref} (° C)	25	T_{NOC} (° C)	40
ρ (kg/m^3)	1.225	η_{w}	0.4
v_{cut-in}(m/s)	5	$v_{cut-out}$(m/s)	35
dr_{w}	0.05	C_{inv}^{s} (€/kW)	1930
C_{om}^{s} (€/kw-year)	20	E_{an}^{s} (kWh/year)	1400
σ^s	0.01	dr_{s}	0.05
n (years)	25	C_{inv}^{w} (€/kW)	3500
C_{om}^{w} (€/Kw-year)	110	E_{an}^{w} (kWh/year)	2000
σ^w	0.01		
Li-ion Battery			
C_{inv}^b(kWh€)	147	C_{om}^b(€/kW-year)	5
u_{es}	0 , 1	dr_b (%)	1
η_{b^+}, η_{b^-}	0.9	SV(€/kWh)	10
I_{b+}^t, I_{b-}^t	1.4	$\eta_{e,app}$	0.8
E_{max} (kWh)	200		
Thermal Storage			
C_{inv}^{th} (€/kWh)	18	C_{om}^{th}(€/kW-year)	3
η_{th^+}, η_{th^-}	0.95	dr_{th}(%)	5
u_{th}	0 , 1	I_{s+}^t, I_{s-}^t	0.7
Ξ_{ref}(kWh)	110		

and $\sum V_{Chp}^t$ influence each of these components. Figs. 7(c) to (f) illustrate the individual impacts of increasing these variables on each cost component. These figures show that greater utilization of PV, wind, battery system, and CHP results in a reduction in electricity costs (C_e) and emission costs (C_c), while leading to an increase in natural gas costs (C_g) and operational costs (C_o). Fig. 7(g) shows the amount of electricity sold to the main grid. In the initial scenarios (up to scenario 15), the microgrid consumes all of its generated power to meet internal demand, resulting in no energy exports. As the capacities of S_{PV}, R_{WT}, E_{max}, and $\sum V_{Chp}^t$ increase, the system begins to generate surplus en-

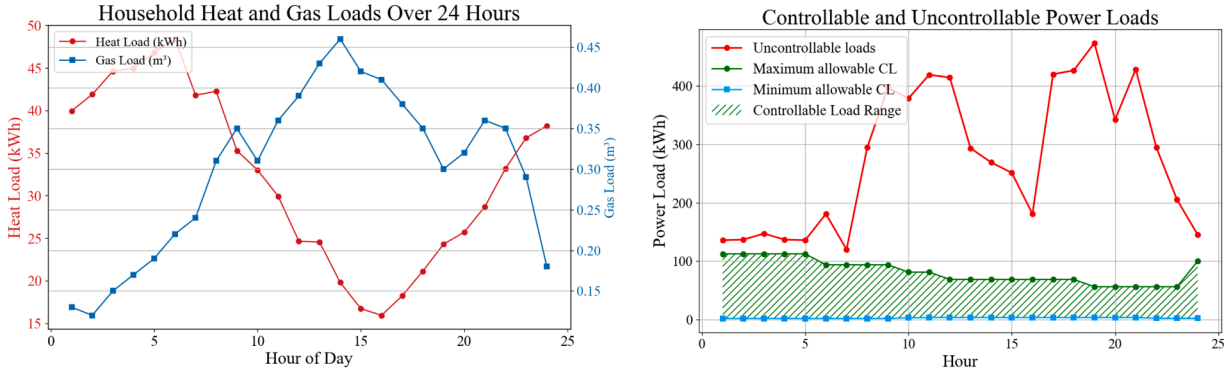

(a) Heat and gas loads.

(b) Controllable and Uncontrollable power loads.

Fig. 5. Various household load types.

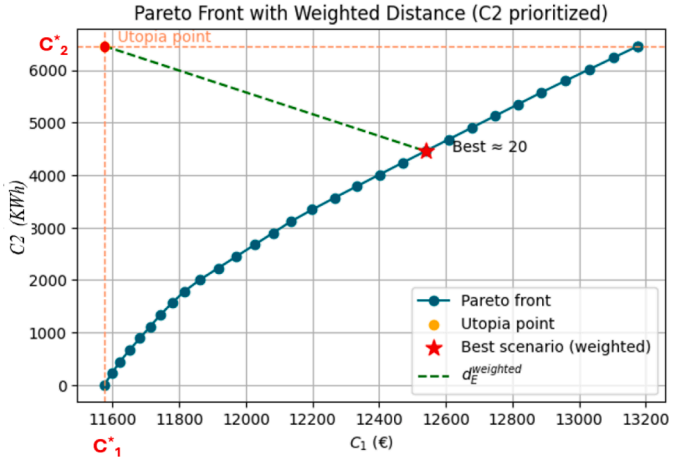

Fig. 6. Pareto front for C1 and C2.

ergy starting from scenario 16, which can then be exported to the main grid.

Gas allocation across the different scenarios is illustrated in Fig. 8. Initially, natural gas is primarily used for direct heating (e.g., through boilers). Up to scenario 10, boiler usage gradually decreases, while gas consumption by the CHP units increases. Eventually, in the later scenarios, all allocated gas is fully utilized by the CHP system. The algorithm operates in a continuous update manner and ultimately identifies the utopia point, which serves as a theoretical ideal representing the best attainable values for each objective function. This point is used as a reference to evaluate and select the optimal scenario. The optimal set of decision variables is obtained by minimizing the euclidean distance from each scenario to the utopia point, as formulated in the optimization Eq. (48) [51]. To reflect the relative importance of each objective in the decision-making process, appropriate weights are assigned. In this study, greater importance is attributed to C_2 compared to C_1. Accordingly, the weights are set to $w_1 = 0.3$ and $w_2 = 0.7$, emphasizing the priority of maximizing C_2 over minimizing C_1 in the multi-objective optimization process.

$$d_E^{weighted} = \sqrt{w_1 \cdot \left(\frac{C_1 - C_1^\star}{C_1^{max} - C_1^\star}\right)^2 + w_2 \cdot \left(\frac{C_2^\star - C_2}{C_2^\star - C_2^{min}}\right)^2} \quad (48)$$

Where, $C_1^\star$ and $C_2^\star$ denote the coordinates of the utopia point corresponding to the objective functions, as illustrated in Fig. 6. The optimization problem, formulated using Eq. (48), identifies the optimal scenario in the vicinity of scenario 20. The bounds imposed on the sizing variables S_{PV}, R_{WT}, E_{max}, and $\sum V_{Chp}^t$, along with their corresponding optimal values, are summarized in Table 3.

3.2.2. Heat and power management under power load uncertainty

Once the optimal values for S_{PV}, R_{WT}, E_{max}, and $\sum V y_{Chp}^t$ are determined, they are integrated into the 14-bus IEEE test system, as depicted in Fig. 9. The objective is to develop a robust energy management strategy that ensures cost-effective scheduling of energy resources. The proposed robust optimization framework addresses uncertainties from uncontrollable power loads and enables reliable planning to meet electricity, heat, and gas demands across various scenarios. The convergence behavior of the optimization process illustrated in Fig. 10 clearly demonstrates the numerical stability and computational efficiency of the proposed MINLP formulation. Within the BARON global optimization framework, the model consistently attains the global optimum while strictly satisfying the predefined optimality tolerances.

Figs. 11 and 12 illustrate the impact of robust optimization on power-related variables and overall system costs. Fig. 11(a) illustrates the variability of uncontrollable demand loads under risk-neutral and robust optimization strategies. The robust approach maintains higher load values during peak periods to account for potential uncertainty deviations, ensuring system reliability. Fig. 11(b) demonstrates how robust optimization reshapes the scheduling of controllable (demand-response) loads, effectively flattening their profile and reducing sudden demand variations. This adjustment enhances system stability and prevents operational stress during uncertain conditions. Fig. 11(c) shows the impact of these uncertainties on electricity transactions with the main grid. Compared to the risk-neutral case, the robust optimization strategy results in higher electricity purchases during critical hours and fewer exports, reflecting a conservative behavior aimed at mitigating the effects of forecast errors and ensuring supply adequacy. Fig. 12 presents a comparative analysis of the main cost components under the robust optimization and risk-neutral approaches, highlighting the influence of uncertainty management on overall system economics. As shown, implementing robust optimization results in an increase in electricity cost, emission cost, and total system cost by approximately 21 %, 15 %, and 6 %, respectively. This increase reflects the conservative nature of the robust strategy, which prioritizes system reliability and feasibility under worst-case uncertainty scenarios. In contrast, the amount of electricity sold to the main grid decreases by nearly 17 %, indicating a shift toward reduced grid dependency and a more secure internal energy balance. Meanwhile, both the gas cost and operational cost remain nearly constant across the two strategies, demonstrating that the impact of uncertainty is primarily concentrated in the electricity-related components.

To assess the influence of the uncertainty radius (α_1) on system performance, three complementary sensitivity analyses were performed: linear, normalized, and elasticity-based analysis, as shown in Fig. 13. Fig. 13(a) shows the linear sensitivity of each cost component, indi-

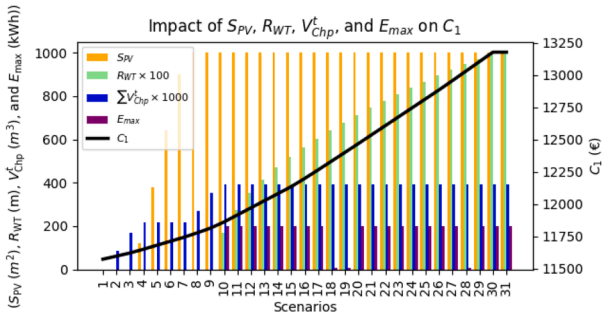

(a) Impact of S_{PV}, R_{WT}, $\sum V^t_{Chp}$, and E_{max} on C_1.

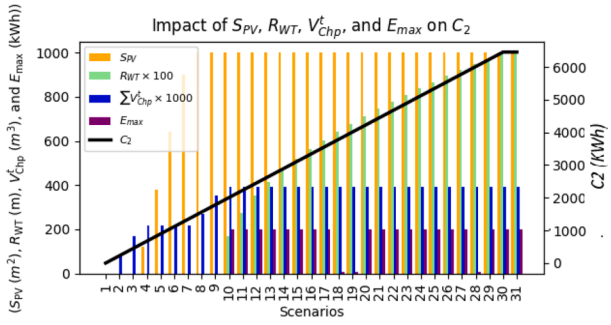

(b) Impact of S_{PV}, R_{WT}, $\sum V^t_{Chp}$, and E_{max} on C_2.

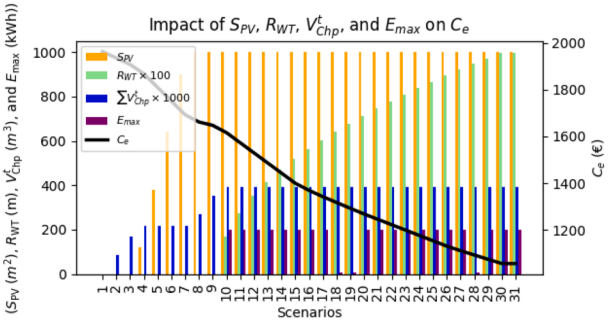

(c) Impact of S_{PV}, R_{WT}, $\sum V^t_{Chp}$, and E_{max} on C_e.

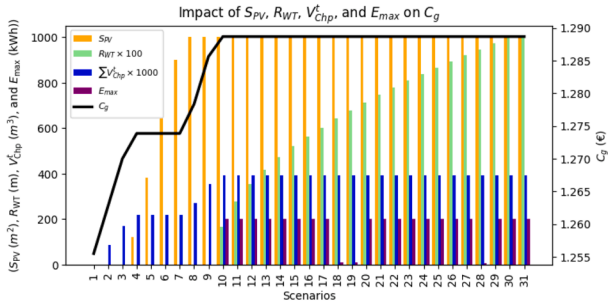

(d) Impact of S_{PV}, R_{WT}, $\sum V^t_{Chp}$, and E_{max} on C_g.

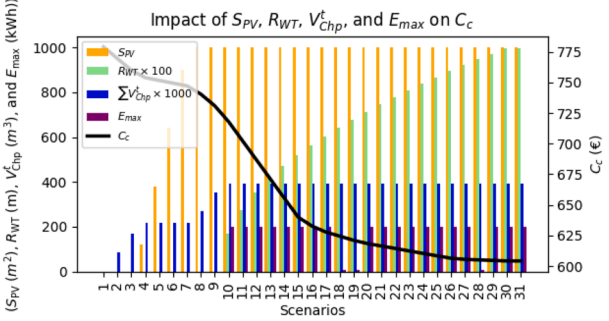

(e) Impact of S_{PV}, R_{WT}, $\sum V^t_{Chp}$, and E_{max} on C_c.

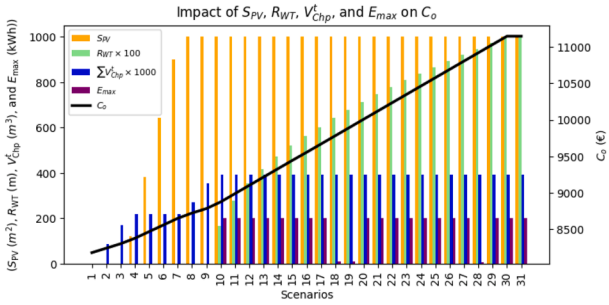

(f) Impact of S_{PV}, R_{WT}, $\sum V^t_{Chp}$, and E_{max} on C_o.

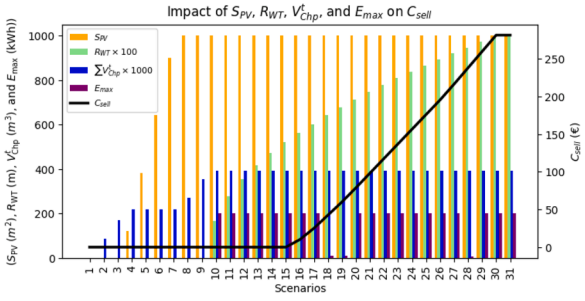

(g) Impact of S_{PV}, R_{WT}, $\sum V^t_{Chp}$, and E_{max} on C_{sell}.

Fig. 7. Impact of sizing variables on various cost components.

Table 3
Bounding and optimal values of decision variables.

Variables	Symbol	Min	Max	Optimal Values
Gas allocation to CHP	$\sum V^t_{Chp}$ (m^3)	0	20	0.39
Surface area of PV panels	S_{PV} (m^2)	0	1100	1030
Radius of wind turbine	R_{WT} (m)	0	10	7.46
Capacity of battery storage	E_{max} (kWh)	0	230	205

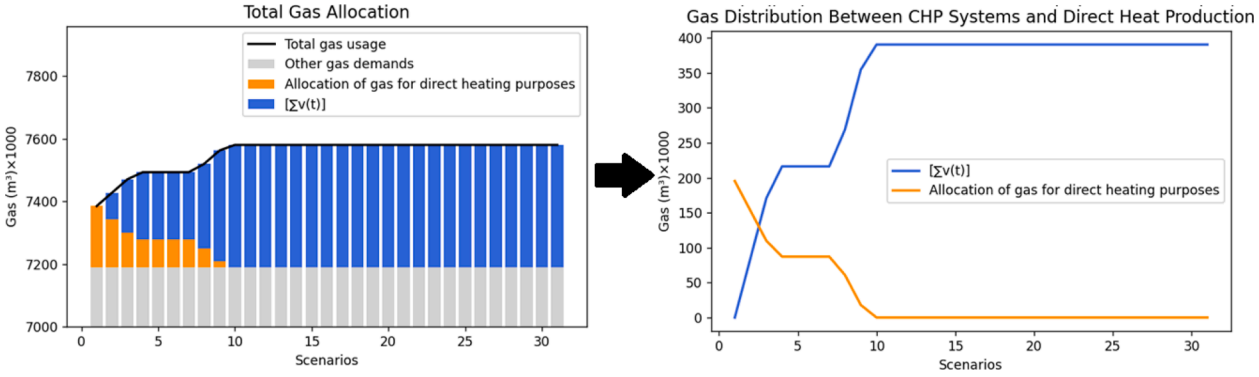

Fig. 8. Impact of S_{PV}, R_{WT}, $\sum V_{Chp}^{t}$, and E_{max} on gas allocation and direct gas from the grid to heating.

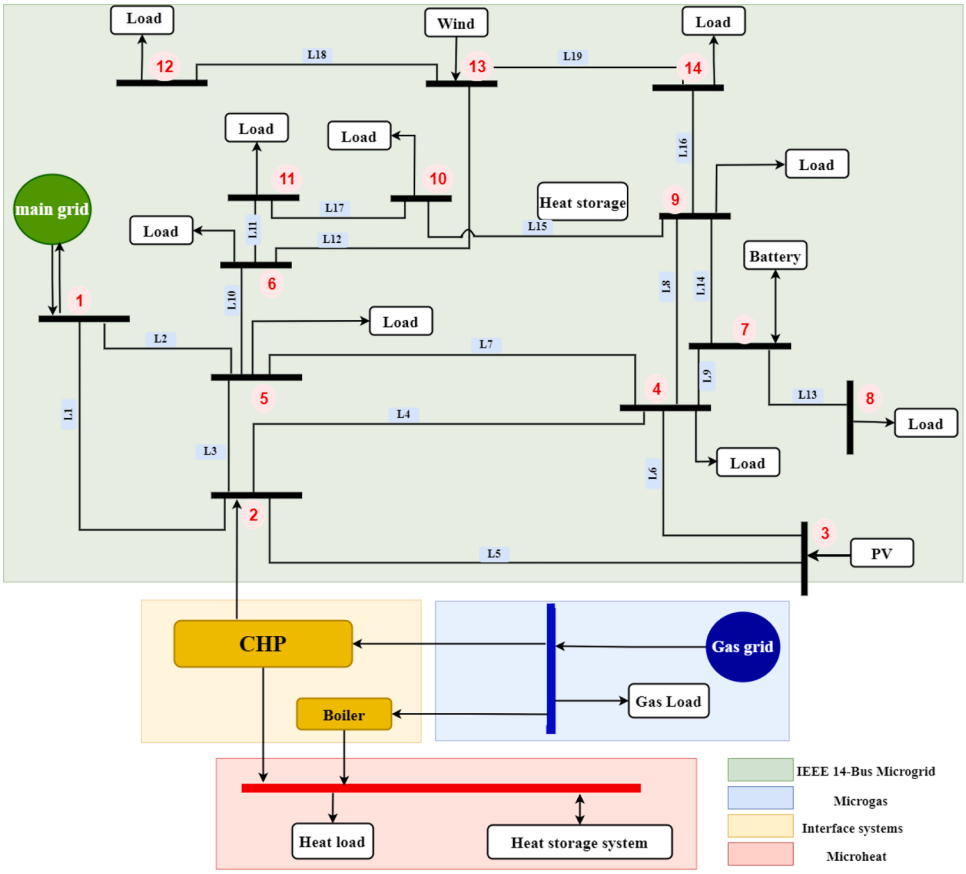

Fig. 9. The 14-bus IEEE microgrid, along with the GDS and DHN.

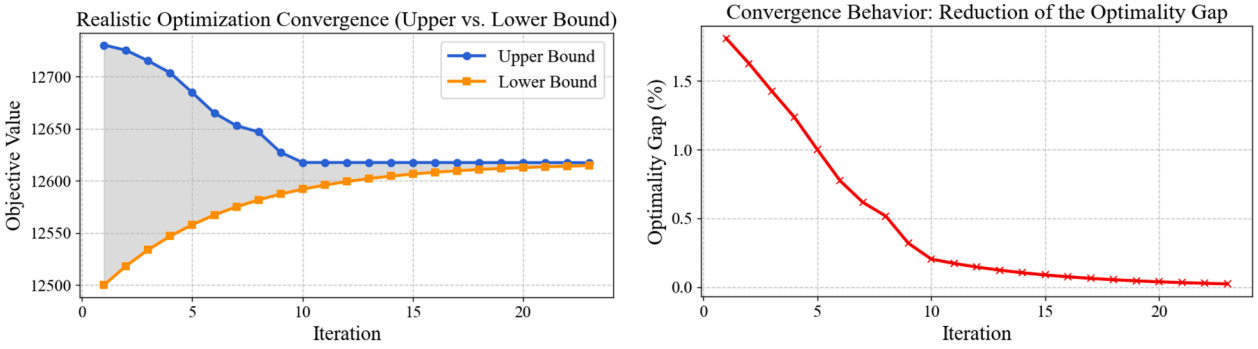

(a) Optimization convergence between upper and lower bounds.

(b) Convergence behavior: reduction of the optimality gap.

Fig. 10. Convergence analysis (a) Evolution of upper and lower bounds across iterations. (b) Reduction of the optimality gap demonstrating global convergence.

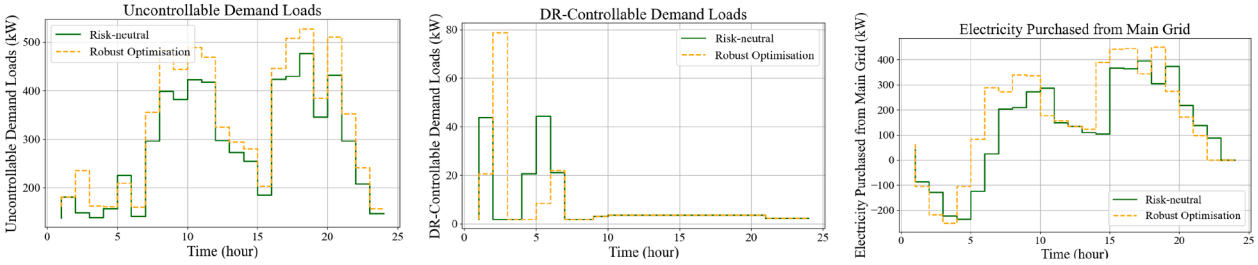

(a) Uncontrollable loads. (b) Controllable loads. (c) Electricity transactions with the main grid.

Fig. 11. Impact of uncertainty in uncontrollable loads and electricity transactions with the main grid.

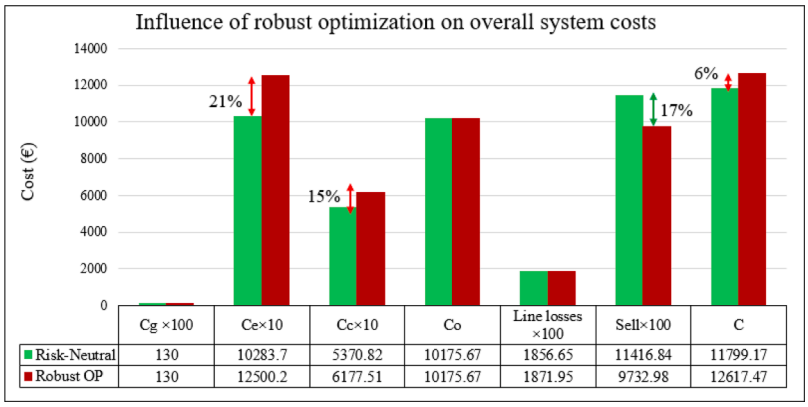

	Cg ×100	Ce×10	Cc×10	Co	Line losses ×100	Sell×100	C
Risk-Neutral	130	10283.7	5370.82	10175.67	1856.65	11416.84	11799.17
Robust OP	130	12500.2	6177.51	10175.67	1871.95	9732.98	12617.47

Fig. 12. Comparison of costs under robust optimization strategy and risk-neutral approach.

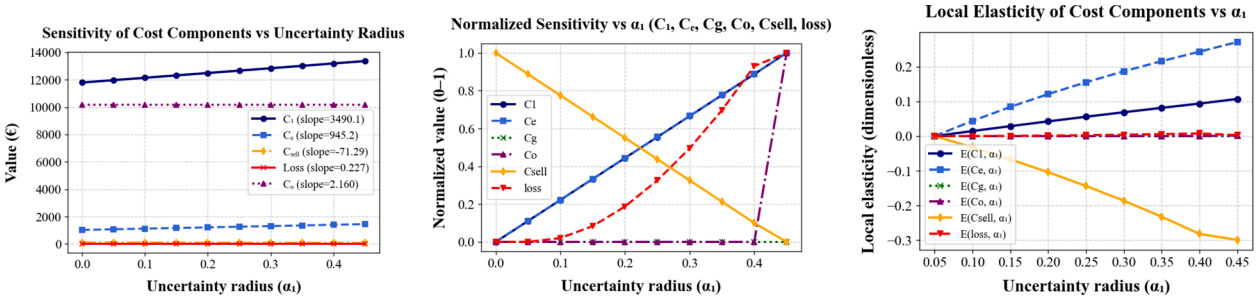

(a) Absolute variation of cost components. (b) Normalized sensitivity (0–1) comparison. (c) Local elasticity of cost components vs. α_1.

Fig. 13. Sensitivity analysis of cost components with respect to the uncertainty radius α_1: (a) Absolute variation of cost components vs. α_1., (b) Normalized relative evolution, and (c) Elasticity-based percentage responsiveness.

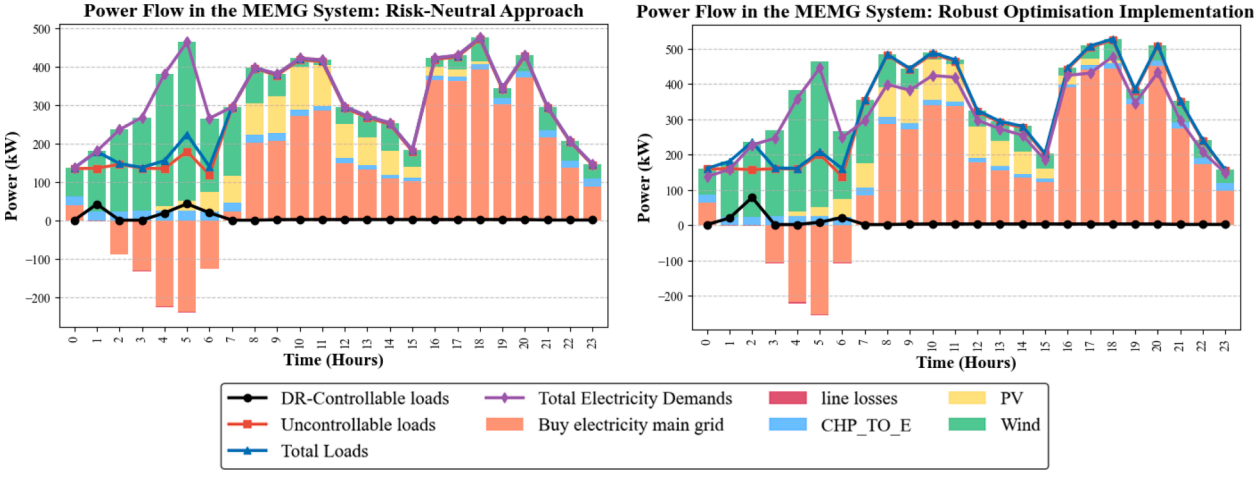

Fig. 14. Power management under risk-neutral and robust optimization approaches.

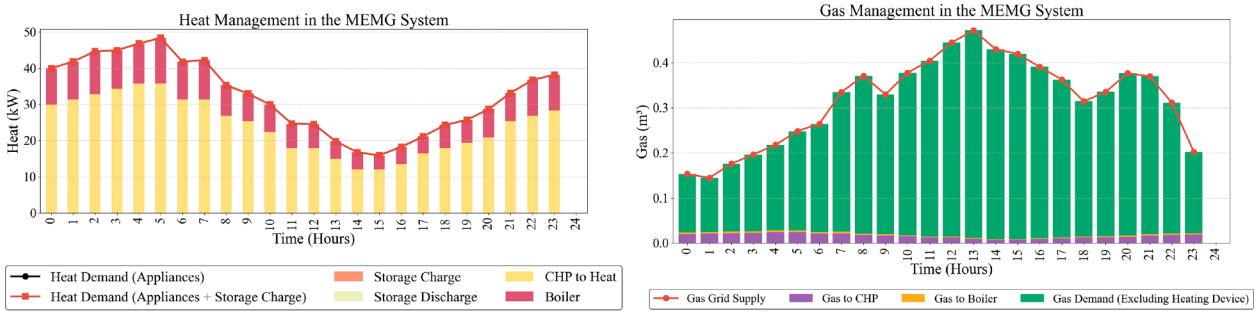

(a) Heat management. (b) Gas management.

Fig. 15. Heat, and gas management in a 14-bus IEEE configuration under robust optimization strategy.

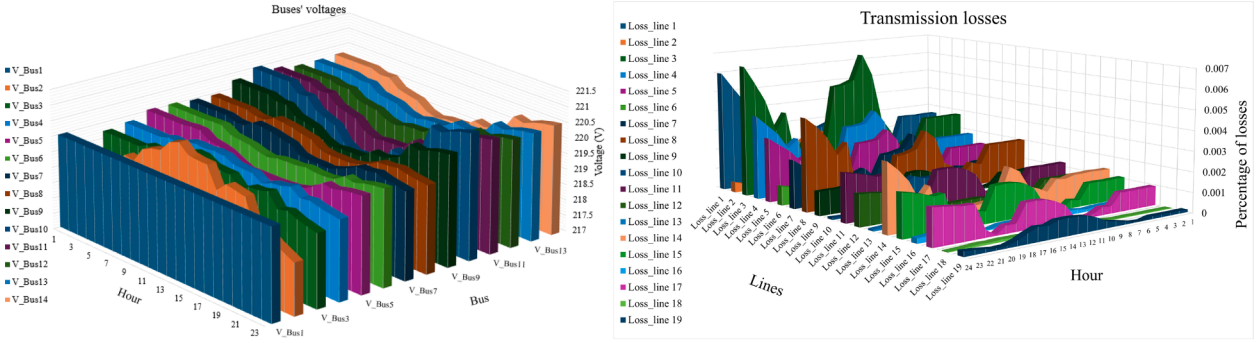

(a) Voltages at the buses. (b) Losses in the transmission lines.

Fig. 16. Voltages at the buses and losses in the transmission lines.

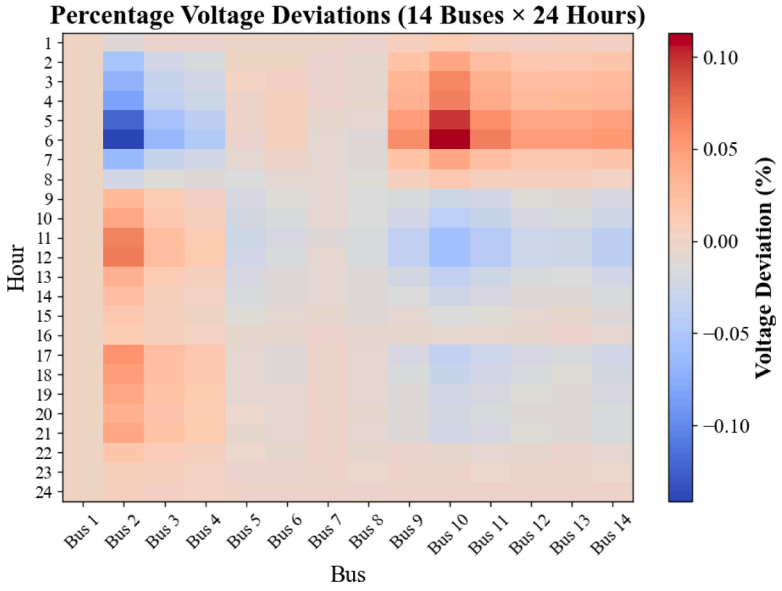

Fig. 17. Voltage deviation percentages for 14 buses over 24 hours.

cating their absolute variation with α_1. Both C_1 and C_e increase almost linearly as uncertainty grows, while C_{sell} decreases, reflecting a more conservative operating strategy. Cost C_o and losses remain nearly constant, showing minimal dependency on uncertainty. Fig. 13(b) presents the normalized sensitivity (0-1 scaling), enabling comparison of relative trends. The results confirm that C_1 and C_e grow consistently with α_1, while C_{sell} declines, illustrating the trade-off between higher costs and reduced revenues. Operating cost (C_o), gas cost (C_g), and losses cost show weak sensitivity. Fig. 13(c) illustrates the local elasticity, which represents the percentage change in each cost for a 1 % change in α_1, and is defined as follows:

$$E(Y,\alpha_1) = \frac{\Delta Y/Y}{\Delta\alpha_1/\alpha_1}.$$

A positive $E(Y,\alpha_1)$ indicates that the component increases with uncertainty, while a negative value represents an inverse trend. Costs C_1 and C_e exhibit the highest positive elasticities, meaning they are the most sensitive to uncertainty expansion. This implies that as uncertainty in-

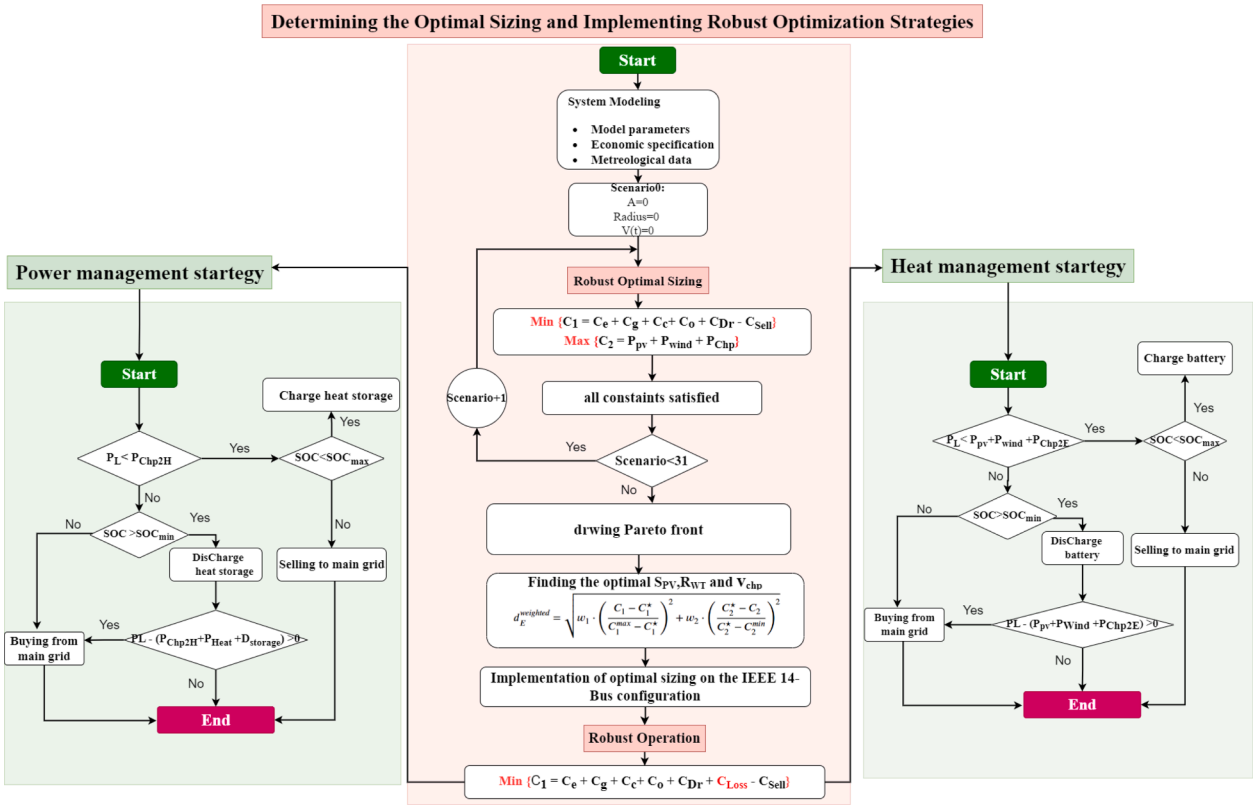

Fig. 18. The process of optimizing system sizing and energy management.

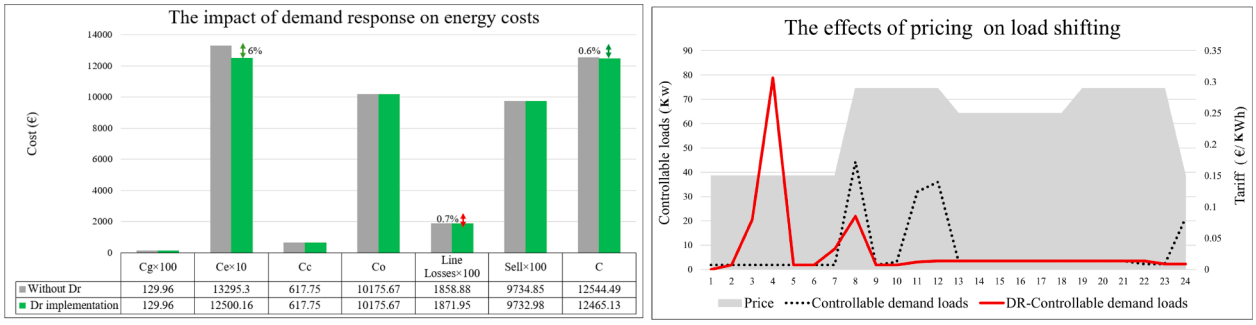

(a) The effect of demand response on costs.

(b) The effect of demand response on load shifting.

Fig. 19. Impact of demand response on costs and load shifting.

creases, the system adopts a more conservative strategy by purchasing additional electricity from the grid and operating more internal resources to ensure reliability, which in turn raises total costs. Grid electricity selling (C_{sell}) shows a negative elasticity, reflecting the system's tendency to reduce grid exports under uncertain conditions to maintain sufficient internal reserves. Both C_o and loss components remain nearly inelastic, indicating limited responsiveness to uncertainty within the examined range.

Figs. 14 and 15 illustrate the impact of robust optimization on power and heat–gas scheduling within the MEMG system, comparing the risk-neutral and robust optimization approaches. In Fig. 14, both cases show that the optimal sizing of S_{PV}, R_{WT}, $E_{\max}$, and $\sum V^{t}_{\mathrm{Chp}}$ ensures that all power demands are satisfied throughout the scheduling horizon. However, notable differences arise in the interaction with the main grid and in resource scheduling patterns. Under the robust optimization approach, the system purchases more electricity from the main grid while selling less compared to the risk-neutral case. This behavior reflects a conservative scheduling strategy that prioritizes reliability and resilience under uncertainty, ensuring sufficient power availability even in worst-case scenarios. Additionally, the robust strategy leads to different controllable load adjustments compared to the risk-neutral approach. Overall, the results confirm that the robust optimization framework enhances operational security and system reliability, at the expense of slightly higher energy imports, thereby achieving a more resilient and uncertainty-tolerant power management strategy. Fig. 15 illustrates that, with optimal sizing, all heat and gas demands are fully met. Moreover, the figure shows that power load uncertainty has a minimal impact on the scheduling of gas and heat resources.

Although this study focuses on hierarchical microgrid control at the tertiary level, where voltage regulation (handled by the primary and secondary levels) is not directly managed, the network constraints are still taken into account. Accordingly, Fig. 16 illustrates the voltage deviations of all buses throughout the 24-hour operating period. Bus 1, acting as the slack bus, maintains a reference voltage of 220 V, while the remaining buses operate within the acceptable range of approximately 218 V-222 V. As shown in Fig. 17, the percentage voltage de-

viations across the network remain minimal, demonstrating that the proposed robust scheduling and power-flow management strategy effectively maintains voltage stability under uncertain operating conditions.

Fig. 18 illustrates the process of resource sizing and the scheduling of power and heating resources. The flowchart is divided into two core components: robust sizing and robust operation. The robust operation component is further divided into electricity and heat management. It provides a clear and concise summary of the key steps carried out in this research.

3.2.3. Demand response implementation

The implementation of demand response programs enables load shifting, which helps reduce electricity costs and enhances grid reliability. In this study, two DR programs are considered: price-based and incentive-based. The price-based DR includes three tariff levels, while the incentive-based program adjusts controllable electrical loads–shifting them forward or backward based on network conditions–to achieve peak shaving. Fig. 19 shows the impact of DR on system costs and load shifting. As illustrated in Fig. 19(a), the implementation of DR results in a 6 % reduction in electricity costs and a 0.6 % decrease in total costs (C_1). Meanwhile, gas costs, emission costs, operational costs, and electricity exports to the grid remain nearly unchanged, while line losses increase slightly by 0.7 %. This strategy not only reduces electricity expenses for consumers but also enhances grid stability and contributes to overall system sustainability. Fig. 19(b) demonstrates how controllable loads shift in response to dynamic pricing. During high-tariff periods (8:00-12:00 and 20:00-23:00), consumption decreases, whereas it increases during low-tariff periods (1:00-8:00). However, since controllable loads account for only 2.4 % of total demand, the overall impact of DR implementation is relatively limited.

4. Conclusion and future prospects

This study presented a comprehensive sizing and energy management framework for a DC microgrid integrating a DHN and a GDS under power load uncertainty. In the sizing stage, a bi-objective robust optimization model was developed to determine the optimal PV surface area, wind turbine radius, battery storage capacity, and gas allocation to the CHP unit. In the second stage, the optimal design parameters obtained from the sizing process were applied to the IEEE 14-bus test system, where a robust energy management strategy was implemented. The results confirmed that the system can operate reliably and efficiently under varying demand conditions. Although the incorporation of robustness led to moderate increases in electricity cost (21 %), emission cost (15 %), and total cost (6 %), it also resulted in a 17 % reduction in electricity exported to the main grid, thereby improving local energy utilization. The sensitivity analysis revealed that C_1 and C_e are the most responsive components to uncertainty expansion. In contrast, C_{sell} exhibited negative elasticity, indicating the system's tendency to reduce grid exports under uncertain conditions. Both C_o and loss components remained nearly inelastic, demonstrating limited responsiveness to variations in uncertainty. Furthermore, the integration of DR programs yielded a 6 % reduction in electricity costs and a 0.6 % decrease in total costs, while gas costs, emission costs, and operational costs remained nearly unchanged, and line losses increased slightly by only 0.7 %. Overall, the proposed approach offers valuable insights into the design and operation of cost-effective, resilient, and sustainable multi-energy microgrids, capable of maintaining reliable performance under power load uncertainty.

Future research can further advance this work in several meaningful directions. While the present study primarily addresses load uncertainty, future investigations should incorporate renewable generation and market price uncertainties to provide a more comprehensive representation of system variability. In addition, consumer behavior in demand response programs–modeled deterministically in this study–can be enhanced through stochastic elasticity modeling to better capture realistic behavioral and market dynamics. To ensure scalability and practical relevance, the proposed framework should be tested on larger and real-world networks beyond the IEEE 14-bus system. Furthermore, to strengthen experimental validation, future work will explore real-time hardware-in-the-Loop (HiL) implementation using OPAL-RT, enabling verification of the proposed model under practical operating conditions. Finally, integrating artificial intelligence (AI) and machine learning (ML) methods offers promising avenues for improving predictive modeling, fault detection, and adaptive control, thereby increasing system resilience, reliability, and efficiency [52]. Expanding the framework to encompass power-to-gas (P2G) and gas-to-power (G2P) technologies–such as electrolyzers and fuel cells–could also enhance energy flexibility, decarbonization, and economic viability in future multi-energy microgrid applications.

Declaration of generative AI and AI-assisted technologies in the writing process

During the preparation of this work the authors used DeepL and ChatGPT in order to improve the grammar and readability of some sentences. After using these tools/services, the authors reviewed and edited the content as needed and take full responsibility for the content of the publication.

CRediT authorship contribution statement

Mojtaba Hadi: Writing – review & editing, Writing – original draft, Visualization, Software, Resources, Methodology, Investigation, Conceptualization; **Elhoussin Elbouchikhi:** Writing – review & editing, Visualization, Validation, Resources, Project administration, Methodology, Funding acquisition, Conceptualization; **Zhibin Zhou:** Writing – review & editing, Visualization, Investigation; **Abdelhakim Saim:** Writing – review & editing, Visualization, Investigation.

Data availability

Data will be made available on request.

Declaration of competing interest

The authors declare that they have no known competing financial interests or personal relationships that could have appeared to influence the work reported in this paper.

Acknowledgements

The authors acknowledge the financial support from ISEN Yncréa Ouest, Nantes and the region of Pays de la Loire in France.

References

[1] M. Hadi, E. Elbouchikhi, Z. Zhou, A. Saim, M. Shafie Khah, P. Siano, H. Rahbarimagham, P. Martí Colom, Artificial intelligence for microgrids design, control, and maintenance: a comprehensive review and prospects, Energy Conver. Manag. X 27 () (2025).

[2] Z. Ullah, H.S. Qazi, A. Alferidi, M. Alsolami, B. Lami, H.M. Hasanien, Optimal energy trading in cooperative microgrids considering hybrid renewable energy systems, Alexandria Eng. J. 86 (2024) 23–33.

[3] P. Kurukuri, M.R. Mohamed, P.H. Raavi, Y. Arya, Optimal planning and designing of microgrid systems with hybrid renewable energy technologies for sustainable environment in cities, Environ. Sci. Pollut. Res. 31 (22) (2024) 32264–32281.

[4] M. Mathew, M.S. Hossain, S. Saha, S. Mondal, M.E. Haque, Sizing approaches for solar photovoltaic-based microgrids: a comprehensive review, IET Energy Syst. Integrat. 4 (1) (2022) 1–27.

[5] M.A. Hannan, M. Faisal, P.J. Ker, R.A. Begum, Z.Y. Dong, C. Zhang, Review of optimal methods and algorithms for sizing energy storage systems to achieve decarbonization in microgrid applications, Renew. Sustain. Energy Rev. 131 (2020) 110022.

[6] S. Garip, S. Ozdemir, Optimization of PV and battery energy storage size in grid-connected microgrid, Appl. Sci. 12 (16) (2022) 8247.

[7] J. Lian, Y. Zhang, C. Ma, Y. Yang, E. Chaima, A review on recent sizing methodologies of hybrid renewable energy systems, Energy Convers. Manage. 199 (2019) 112027.

[8] G. Ma, J. Li, X.-P. Zhang, A review on optimal energy management of multimicrogrid system considering uncertainties, IEEE Access 10 (2022) 77081–77098.

[9] Z. Shi, T. Zhang, Y. Liu, Y. Feng, R. Wang, S. Huang, Optimal design and operation of islanded multi-microgrid system with distributionally robust optimization, Electr. Power Syst. Res. 221 (2023) 109437.

[10] H. Karimi, S. Jadid, Optimal energy management for multi-microgrid considering demand response programs: a stochastic multi-objective framework, Energy 195 (2020) 116992.

[11] L. Wang, B. Zhang, Q. Li, W. Song, G. Li, Robust distributed optimization for energy dispatch of multi-stakeholder multiple microgrids under uncertainty, Appl. Energy 255 (2019) 113845.

[12] R. Zhang, Y. Chen, Z. Li, T. Jiang, X. Li, Two-stage robust operation of electricity-gas-heat integrated multi-energy microgrids considering heterogeneous uncertainties, Appl. Energy 371 (2024) 123690.

[13] Y.-R. Lee, H.-J. Kang, M.-K. Kim, Optimal operation approach with combined BESS sizing and PV generation in microgrid, IEEE Access 10 (2022) 27453–27466.

[14] M.K. Kiptoo, M.E. Lotfy, O.B. Adewuyi, A. Conteh, A.M. Howlader, T. Senjyu, Integrated approach for optimal techno-economic planning for high renewable energy-based isolated microgrid considering cost of energy storage and demand response strategies, Energy Convers. Manage. 215 (2020) 112917.

[15] X. Li, G. Jones, Optimal sizing, location, and assignment of photovoltaic distributed generators with an energy storage system for islanded microgrids, Energies 15 (18) (2022) 6630.

[16] G. Ma, G. Xu, Y. Chen, R. Ju, Multi-objective optimal configuration method for a standalone wind–solar–battery hybrid power system, IET Renew. Power Gener. 11 (1) (2017) 194–202.

[17] M. Hadi, E. Elbouchikhi, Z. Zhou, A. Saim, Optimal sizing and energy management for multi-Energy microgrids integrated with combined heat and power unit, in: 2025 International Conference on Control, Automation and Diagnosis (ICCAD), IEEE, 2025, pp. 1–6.

[18] M. Hadi, E. Elbouchikhi, Z. Zhou, A. Saim, M. Machmoum, Sizing and energy management in an islanded DC microgrid, in: EPJ Web of Conferences, 326, EDP Sciences, 2025, p. 05001.

[19] K. Sivakumar, R. Jayashree, K. Danasagaran, Efficiency-driven planning for sizing of distributed generators and optimal construction of a cluster of microgrids, Eng. Sci. Technol., Int. J. 24 (5) (2021) 1153–1167.

[20] F.A. Kassab, B. Celik, F. Locment, M. Sechilariu, S. Liaquat, T.M. Hansen, Optimal sizing and energy management of a microgrid: a joint MILP approach for minimization of energy cost and carbon emission, Renew. Energy 224 (2024) 120186.

[21] N. Shirzadi, F. Nasiri, U. Eicker, Optimal configuration and sizing of an integrated renewable energy system for isolated and grid-connected microgrids: the case of an urban university campus, Energies 13 (14) (2020) 3527.

[22] F. Xu, J. Liu, S. Lin, Q. Dai, C. Li, A multi-objective optimization model of hybrid energy storage system for non-grid-connected wind power: a case study in china, Energy 163 (2018) 585–603.

[23] A. Berrueta Irigoyen, M. Heck, M. Jantsch, A. Ursúa Rubio, P. Sanchis Gúrpide, Combined dynamic programming and region-elimination technique algorithm for optimal sizing and management of lithium-ion batteries for photovoltaic plants, Appl. Energy, 228 (2018) 1–11 (2018).

[24] S. Mohseni, R. Khalid, A.C. Brent, Stochastic, resilience-oriented optimal sizing of off-grid microgrids considering EV-charging demand response: an efficiency comparison of state-of-the-art metaheuristics, Appl. Energy 341 (2023) 121007.

[25] M.E. Sallam, M.A. Attia, A.Y. Abdelaziz, M.A. Sameh, A.H. Yakout, Optimal sizing of different energy sources in an isolated hybrid microgrid using turbulent flow water-based optimization algorithm, IEEE Access 10 (2022) 61922–61936.

[26] R. Xie, W. Wei, M. Shahidehpour, Q. Wu, S. Mei, Sizing renewable generation and energy storage in stand-alone microgrids considering distributionally robust shortfall risk, IEEE Trans. Power Syst. 37 (5) (2022) 4054–4066.

[27] F. Boutros, M. Doumiati, J.-C. Olivier, I. Mougharbel, H. Kanaan, New modelling approach for the optimal sizing of an islanded microgrid considering economic and environmental challenges, Energy Convers. Manage. 277 (2023) 116636.

[28] M. Gholami, S.A. Mousavi, S.M. Muyeen, Enhanced microgrid reliability through optimal battery energy storage system type and sizing, IEEE Access 11 (2023) 62733–62743.

[29] M. Hadi, E. Elbouchikhi, Z. Zhou, A. Saim, Optimal energy management in multi energy microgrid with combined heat and power system and demand side response integration, Renew. Energy 256 (2026) 124076. https://doi.org/10.1016/j.renene.2025.124076

[30] F. Bagheri, H. Dagdougui, M. Gendreau, Stochastic optimization and scenario generation for peak load shaving in smart district microgrid: sizing and operation, Energy Build. 275 (2022) 112426.

[31] A.M. Jasim, B.H. Jasim, F.-C. Baiceanu, B.-C. Neagu, Optimized sizing of energy management system for off-grid hybrid solar/wind/battery/biogasifier/diesel microgrid system, Mathematics 11 (5) (2023) 1248.

[32] M.K. Darabi, H.G. Ganjehlou, A. Jafari, M. Nazari-Heris, G.B. Gharehpetian, M. Abedi, Evaluating the effect of demand response programs (DRPs) on robust optimal sizing of islanded microgrids, Energies 14 (18) (2021) 5750.

[33] A. Emrani, Y. Achour, M.J. Sanjari, A. Berrada, Adaptive energy management strategy for optimal integration of wind/PV system with hybrid gravity/battery energy storage using forecast models, J. Energy Storage 96 (2024) 112613.

[34] W. Nemouchi, Y. Amrane, H. Nemouchi, N.L. Boucetta, Energy management for optimal design of PV/wind/diesel system for water pumping irrigation in semi-arid climate, Energy Convers. Manage. 304 (2024) 118216.

[35] A. Chrif, E. Elbouchikhi, A. Abouloifa, M. Machmoum, Techno-economic sizing and multi-objective energy management of AC multi-bus microgrids for enhanced reliability and cost efficiency: application to small villages in morocco, Energy Conver. Manag.: X (2025) 101246.

[36] M.F. Zia, E. Elbouchikhi, M. Benbouzid, Optimal operational planning of scalable DC microgrid with demand response, islanding, and battery degradation cost considerations, Appl. Energy 237 (2019) 695–707.

[37] X. Gao, K. Li, Y.-c. Cao, G.J. Offer, H. Wang, Simulation and understanding of degraded lithium-ion battery self-heating ignition, Appl. Energy 384 (2025) 125435.

[38] J. Mitali, S. Dhinakaran, A.A. Mohamad, Energy storage systems: a review, Energy Storage Sav. 1 (3) (2022) 166–216.

[39] J. You, J. Gao, R. Li, R. Wang, Z. Xu, Air-source heat pump assisted absorption heat storage for discharging under low ambient temperature, Appl. Energy 380 (2025) 125121.

[40] O. Erixno, N. Abd Rahim, F. Ramadhani, N.N. Adzman, Energy management of renewable energy-based combined heat and power systems: a review, Sustainable Energy Technol. Assess. 51 (2022) 101944.

[41] M.A. Bagherian, K. Mehranzamir, A comprehensive review on renewable energy integration for combined heat and power production, Energy Convers. Manage. 224 (2020) 113454.

[42] S. Gao, H. Li, Y. Hou, J. Yan, Benefits of integrating power-to-heat assets in CHPs, Appl. Energy 335 (2023) 120763.

[43] A. Nawaz, M. Zhou, J. Wu, C. Long, A comprehensive review on energy management, demand response, and coordination schemes utilization in multi-microgrids network, Appl. Energy 323 (2022) 119596.

[44] S. Mandal, K.K. Mandal, Optimal energy management of microgrids under environmental constraints using chaos enhanced differential evolution, Renew. Energy Focus 34 (2020) 129–141.

[45] A.K. Erenoğlu, İ. Şengör, O. Erdinç, A. Taşcıkaraoğlu, J.P.S. Catalão, Optimal energy management system for microgrids considering energy storage, demand response and renewable power generation, Int. J. Elec. Power Energy Syst. 136 (2022) 107714.

[46] S. Nikolina, International renewable energy agency (IRENA) (2016).

[47] Y. Amry, E. Elbouchikhi, F. Le Gall, M. Ghogho, S. El Hani, Optimal sizing and energy management strategy for EV workplace charging station considering PV and flywheel energy storage system, J. Energy Storage 62 (2023) 106937.

[48] RTE France, La production d'électricité par filière, 2023, (https://www.rte-france.com/eco2mix/la-production-delectricite-par-filiere). Accessed: 2024-05-26.

[49] Joint Research Centre (JRC), European Commission, PVGIS: Photovoltaic Geographical Information System, 2024, (https://re.jrc.ec.europa.eu/pvg_tools/en/tools.html#PVP). Accessed: 2024-05-26.

[50] International Renewable Energy Agency (IRENA), Renewable power generation costs in 2023, International Renewable Energy Agency, Abu Dhabi, 2024.

[51] N. Gunantara, A review of multi-objective optimization: methods and its applications, Cogent Eng. 5 (1) (2018) 1502242.

[52] B.K. Reddy, N.C. Giri, P.K. Yemula, E.B. Agyekum, Y. Arya, Optimal operation of cogeneration power plant integrated with solar photovoltaics using dls-WMA and ANN, Int. J. Energy Res. 2024 (1) (2024) 5562804.